The Warm Ionized Medium: Distribution, Kinematics, and Physical Conditions

by

L. Matthew Haffner

A dissertation submitted in partial fulfillment of the
requirements for the degree of

Doctor of Philosophy
(Astronomy)

at the

University of Wisconsin – Madison

1999

© Copyright 1999 by L. Matthew Haffner
All rights reserved.

For Grandpa

"Minds are like parachutes; they work best when open."
—Lord Thomas Dewar

Acknowledgments

The opportunity to work on the WHAM project has been the most exciting of my scientific career. Thanks go first and foremost to Ron Reynolds for giving me the chance to work on the WHAM team and the opportunity to help define so much of the software development. Steve Tufte also deserves endless gratitude for putting up with countless discussions about esoteric details and for providing excellent feedback. The smooth sailing of the project rests entirely on the shoulders of Kurt Jaehnig and Jeff Percival for providing some of the best hardware and software engineering I have ever had the privilege to use.

Finally, thanks to my family and friends, for providing the inspiration and encouragement to pursue a scientific career; to my parents, for developing my love for learning; and to Kristina, for her patience, understanding, and many lonely nights while I was observing.

Contents

Introduction ix
References . . . xi

1 The Wisconsin H-Alpha Mapper All Sky Survey 1
Abstract . . . 2
1.1 Advantages of the WHAM Survey . . . 3
1.2 The WHAM Instrument . . . 3
1.3 Survey Strategies . . . 4
1.4 Survey Operations . . . 5
1.5 Data Reduction . . . 5
1.5.1 Creating Spectra . . . 5
1.5.2 Assembling Maps . . . 8
1.6 The Hα Sky . . . 9
References . . . 10

2 WHAM observations of Hα, [S II], and [N II] 17
Abstract . . . 18
2.1 Introduction . . . 19
2.2 Observations . . . 19
2.3 Results . . . 20
2.3.1 Overview . . . 20
2.3.2 Scale Height of the WIM . . . 21
2.3.3 Line Ratios . . . 22
2.4 Discussion . . . 22
2.4.1 Physical Parameters of the WIM . . . 22
2.4.2 A Faint, Diffuse H II Region . . . 25
2.5 Summary . . . 28
References . . . 29

3 Faint, Large-scale Hα Filaments in the Milky Way 45
Abstract . . . 46
3.1 Introduction . . . 47
3.2 Observations . . . 47
3.3 Results . . . 48
3.4 Discussion . . . 49
References . . . 52

A Technical Summary of WHAM Communications and Operations **57**
A.1 Introduction 57
A.1.1 Hardware Overview 57
A.1.2 Software Overview 58
A.2 The Interface Layer 59
A.3 The C & C Layer 60
A.4 The User Layer 60

List of Tables

1.1 Atmospheric Lines near Hα 11

2.1 Atmospheric Lines in [S II] and [N II] Observations 30

3.1 Fitted Filament Parameters 53

List of Figures

1.1 Steps in WHAM data reduction . . . 12
1.2 An example observing plan: Hα Survey . . . 13
1.3 An example observing plan: [S II] observations . . . 14
1.4 A portion of the Hα sky . . . 15

2.1 Hα Emission from the Orion Arm . . . 31
2.1 (cont.) Hα Emission from the Perseus Arm . . . 32
2.2 Sample Hα Spectra . . . 33
2.3 $\ln I_{\mathrm{H}\alpha}$ vs. $\tan b$: Scale height of WIM emission . . . 34
2.4 Emission Line Ratio Maps: -10 to $+10$ km s^{-1} . . . 35
2.5 Emission Line Ratio Maps: -50 to -30 km s^{-1} . . . 36
2.6 [S II]/Hα vs. Hα: Local and Perseus arms . . . 37
2.7 [N II]/Hα vs. Hα: Local and Perseus arms . . . 38
2.8 [S II]/Hα vs. [N II]/Hα: Local and Perseus arms . . . 39
2.9 $\ln I$ vs. $\tan b$: Line intensities and ratios in the Local arm . . . 40
2.10 $\ln I$ vs. $\tan b$: Line intensities and ratios in the Perseus arm . . . 41
2.11 [S II]/Hα vs. [N II]/Hα: Local arm with T, S$^+$/S grid . . . 42
2.12 [S II]/Hα vs. [N II]/Hα: Perseus arm with T, S$^+$/S grid . . . 43
2.13 $\ell = 131^\circ$ and $b = -11^\circ$ Profiles: -10 to $+10$ km s^{-1} . . . 44

3.1 A portion of the WHAM Hα Sky Survey . . . 54
3.2 Longitude-Velocity intensity map at $b = +25^\circ$ . . . 55
3.3 Filament and background spectra at $b = +25\overset{\circ}{.}5$ . . . 56

A.1 Layout of the WHAM network . . . 63
A.2 Conceptual model of the WHAM software system . . . 64
A.3 The WHAM telemetry text tool . . . 65
A.4 The WHAM launching widget . . . 65
A.5 The WHAM liquid nitrogen filling widget . . . 66
A.6 The WHAM MCS Information widget . . . 66
A.7 The WHAM gas pressure system widget . . . 67
A.8 The WHAM CCD camera widget . . . 67
A.9 The WHAM telescope pointer widget . . . 68
A.10 The WHAM star finder widget . . . 68
A.11 The WHAM telescope pointing paddle widget . . . 69
A.12 The WHAM mechanism control widget . . . 69
A.13 The WHAM etalon tuning widget . . . 70
A.14 The WHAM observation planning widget . . . 70
A.15 Example planning plot for the night of June 18 . . . 71
A.16 WHAM sky coverage . . . 72
A.17 The WHAM survey client . . . 73

Introduction

With a scale height of 1 kpc, mass surface density equal to one-third that of H I, and power input requirement equal to the supernovae output rate of our Galaxy (Reynolds 1993), the Warm Ionized Medium (WIM) is justifiably a major component of the Interstellar Medium (ISM). Although, originally discovered in the 1960s through radio observations (Hoyle & Ellis 1963; Guélin 1974), the WIM is typically studied through optical emission lines, particularly Hα, [S II] λ6716, and [N II] λ6583. Characterizing the details of the WIM is important not only for improving the picture of the ISM and the interaction among its components, but also for understanding the nature of the foreground gas through which all extragalactic and cosmological observations are made.

Several authors have presented ideas for the source of the ionizing power of the WIM. Most recently, Miller & Cox (1993) and Dove & Shull (1994) present a picture of a pervasive, warm, (originally) neutral medium being ionized by radiation from early-type stars leaking between cold H I clouds or out of density bounded H II regions. This picture results in regions of fully ionized gas and "shadowed" neutral gas. Other theories suggest that the Hα emission should be positively correlated with H I features. Norman (1991) and Koo, Heiles, & Reach (1992) associate the pervasive Hα emission with the walls of superbubbles, "chimneys," and "worms," while McKee & Ostriker (1977) suggest that prominent Hα emission is confined to the surface of neutral clouds bathed in a hot medium. Alternatively, Spitzer & Fitzpatrick (1993) and Sciama (1990) have suggested that the H^+ should be well-mixed with the neutral material.

Major advances in detector technology have recently allowed breakthrough studies of the WIM. Direct measurement of extremely faint, optical diagnostic lines in the WIM, including He I λ5876 (Tufte 1997) and [O I] λ6300 (Reynolds et al. 1998), are beginning to place important constraints on the nature and source of the ionization and heating of this gas in our Galaxy. The most comprehensive work on an edge-on spiral galaxy similar to the Milky Way has been undertaken by Rand (1997; 1998), who has measured numerous emission lines in the halo of NGC 891. Domgörgen & Dettmar (1997) and Golla, Dettmar, & Domgörgen (1996) have also probed similar lines in the edge-on galaxies NGC 2188 and NGC 4631. All found a pronounced increase in the intensity ratios [S II]/Hα and [N II]/Hα in regions with fainter Hα emission. For spectra obtained perpendicular to the galaxies, these ratios rise systematically with distance from the galactic plane. Ferguson, Wyse, & Gallagher (1996) studied the highly-inclined SBm galaxy NGC 55 and found a smooth transition in the emission-line ratios of [O II]/(Hα+[N II]) and [S II]/(Hα+[N II]) from bright H II regions to faint WIM-like gas. In addition, several imaging surveys are now underway to map the details of the structure of faint Hα emission near the plane of the Milky Way (Dennison, Topasna, & Simonetti 1998); Gaustad, et al. 1997; Parker & Phillips 1998).

Utilizing this new CCD technology, we have designed and built a dedicated survey instrument, the Wisconsin H-Alpha Mapper (WHAM), to produce the first deep, velocity-resolved maps of the WIM in our Galaxy. This thesis describes the nature of the survey and presents some initial results from it. Chapter 1 introduces the survey methodology,

operations, and data. A brief overview of the technical operation of WHAM is included here with more detailed coverage in Appendix A. Complete reduction of WHAM data from CCD images to spectra to maps is explained and a portion of the all sky Hα map is presented. Chapter 2 combines a section of these Hα data with [S II] and [N II] observations of the same region to explore physical parameters of the WIM. In Chapter 3 we present an example of a dramatic set of Hα filaments in the halo of the Milky Way.

References

Dennison, B., Simonetti, J. H., & Topasna, G. A. 1998, PASA, 15, 147

Domgörgen, H. & Dettmar, R.-J. 1997, å, 322, 391

Dove, J. B. & Shull, J. M. 1994, ApJ, 430, 222

Gaustad, J., McCullough, P., Van Buren, D. 1996 PASP, 108, 351

Golla, G., Dettmar, R.-J. & Domgörgen, H. 1996, A&A, 313, 439

Guèlin, in IAU Symposium No. 60: Galactic Radio Astronomy, eds. F. J. Kerr & S. C. Simonson (Dordrecht:Ridel), 51

Hoyle, F. & Ellis, G. R. 1963, Australian J. Phys, 16, 1

Ferguson, A. M. N., Wyse, R. F. G., Gallagher, J. S. 1996, AJ, 112, 2567

Koo, B.-C., Heiles, C., & Reach, W. T. 1992, ApJ, 390, 108

McKee, C. F., & Ostriker, J. P. 1977, ApJ, 218, 148

Miller, W. W., III, & Cox, D. P. 1993, ApJ, 417 579

Norman, C. A. 1991, in IAU Symp. 144, The Interstellar Disk-Halo Connection in Galaxies, ed. H. Bloemen (Dordrecht: Kluwer), 337

Parker, Q. A. & Phillips, S. 1998, PASA, 15, 28

Rand, R. J. 1997, ApJ, 474, 129

Rand, R. J. 1998, ApJ, 501, 137

Reynolds, R. J. 1993, in Back to the Galaxy, AIP Proc. 278, eds. S. S. Holt & F. Verter (New York: AIP), 156

Reynolds, R. J., Hausen, N. R., Tufte, S. L. 1998, & Haffner, L. M. 1998, ApJ, 494, L99

Sciama, D.W. 1990, ApJ, 364, 549

Spitzer, L., Jr. & Fitzpatrick, E. L. 1993 ApJ, 409, 299

Tufte, S. L. 1997, PhD Thesis, University of Wisconsin–Madison

Chapter 1

The Wisconsin H-Alpha Mapper All Sky Survey

Abstract

The Wisconsin H-Alpha Mapper (WHAM) has surveyed interstellar Hα emission over the entire northern sky. In the spectral configuration used for the survey, WHAM produces maps with one-degree spatial resolution and 12 km s^{-1} velocity resolution covering approximately $\pm$100 km s^{-1} around the Local Standard of Rest (LSR). This chapter presents the rationale for the survey strategy, the efficient methodology that resulted in completing the survey in 18 months, and the details of how the data are reduced. We also present a region of the Hα sky that has been reduced as a part of the early results from the survey.

1.1 Advantages of the WHAM Survey

The WHAM Hα Sky Survey provides the first Northern Hemisphere, velocity-resolved map of Hα emission from our Galaxy. The primary portion of the survey with $\delta > -20^\circ$ was completed in early 1998, with an additional extension to $\delta = -30^\circ$ completed in the Fall 1998. Although current Hα imaging surveys (Dennison, et al. 1998; Gaustad et al. 1997; Parker & Phillips 1998) will provide moderate to high angular resolution ($\lesssim 1'$), they lack the deep sensitivity needed to map Hα over the entire high latitude sky and they lack velocity resolution. WHAM complements these imaging surveys nicely by providing 12 km s^{-1} resolution with one-degree angular resolution down to sensitivity limits of 0.2 R (1 R; 1 R = $10^6/4\pi$ ph cm^{-2} s^{-1}). The addition of this capability allows the WHAM survey to add two important pieces to the diffuse Hα picture.

First, at this velocity resolution, Galactic Hα emission can be separated from the geocoronal Hα emission from the earth's upper atmosphere, the "geocoronal" Hα line. Since Galactic emission from most regions of the sky is shifted 20–30 km s^{-1} away from the atmospheric line at some time during the year (due to orbital motion of the earth), prudent observing tactics and accurate subtraction of the geocoronal emission make possible an absolute intensity calibration of the interstellar Hα in the WHAM survey. Since the intensity of this foreground emission is comparable to or brighter than the interstellar emission and varies with both time and direction on the sky, normal filter imaging techniques cannot inherently provide a consistent zero-point reference for absolute calibration.

More importantly, velocity resolution will give us the unique opportunity to explore the actual kinematics of the Warm Ionized Medium (WIM) and other extended diffuse Hα sources. Without this resolution, comparing structures found in the WIM with other surveys, particularly H I, is difficult (*e.g.* Reynolds et al. 1995). Our hope is that such comparisons may help reveal the relationships between the WIM and other components of the interstellar medium and narrow the options for sources able to maintain the warm, ionized state of this pervasive gas.

In §1.2, we provide a brief overview of the WHAM instrument. §1.3 and §1.4 describe the strategies and operation of the Hα survey. §1.5 introduces our data reduction techniques. Finally, §1.6 presents maps of the survey data that have been reduced so far.

1.2 The WHAM Instrument

Due to the extended nature of the WIM, large-aperture Fabry-Perot detection techniques have proven to be quite successful in studying the WIM (Reynolds et al. 1990). For WHAM, a 6-inch, dual-etalon Fabry-Perot spectrometer delivers the high-efficiency, high-resolution observations. The dual-etalon design provides superior order rejection over single-etalon systems to achieve a much larger free spectral range while maintaining high spectral resolution (12 km s^{-1}). An all-sky siderostat housing a 0.6-meter lens guides light to the etalon chambers in an environmentally controlled trailer. The center wavelength of the 200 km s^{-1} spectral window is selected by changing the pressure of a high index of refraction gas (SF_6) in sealed etalon chambers. A narrow-band ($\sim$ 20 Å FWHM) interference filter provides additional spectral isolation near the desired wavelength. The resulting spectrum, in the form of a Fabry-Perot ring pattern, is imaged onto a cryogenically cooled Tek 1024×1024 CCD.

The spectrum covers a 200 km s^{-1} interval at 12 km s^{-1} spectral resolution. Coatings on the etalons and optics allow the placement of the 200 km s^{-1} wide spectral window anywhere between 4800 and 7300 Å. In this "spectral mode," the image contains only the average spectrum within the one-degree diameter circular beam, avoiding confusion between

spectral features and angular structures of the source (or stars) within the beam. WHAM also has a set of optics that can be placed in the post-etalon beam to provide an extremely narrow-band (12-200 km s^{-1}), $1'$ angular resolution *image* of the sky within a one-degree field of view. Only the spectral mode (with one-degree angular resolution) is used for the Hα Sky Survey observations presented here. Further details on the WHAM spectrometer and its calibration can be found in Tufte (1997).

WHAM is currently located at Kitt Peak National Observatory. Using the WIYN messaging system designed by Percival (1994, 1995) and custom hardware designed by the *Space Astronomy Lab* at Wisconsin, WHAM is a completely remotely operated telescope system. All functions of the siderostat and spectrometer are routinely operated from our Wisconsin offices. Details on the hardware and software used to operate WHAM and to automate the survey can be found in Appendix A.

1.3 Survey Strategies

The survey consists of more than 37,000 pointings of the one-degree beam with $\Delta b = 0.^\circ85$ and $\Delta l = 0.^\circ98/\cos b$ with $\delta \geq -30^\circ$. The origin of the longitude gridding is offset by $(0.^\circ98/2)/\cos b$ between adjacent latitude rows. This odd spacing achieves nearly full sky coverage near the Galactic plane by nesting the beams. At higher latitudes, some "slipping" of the rows begins to occur and slightly larger gaps are left between adjacent latitude rows. Since the goal is to probe the extended emission of the WIM, these gaps have little effect on the completeness of the survey. To organize these observations, the individual pointings are grouped into observational "blocks." Each block consists of up to 49 one-degree pointings, typically in a 7×7 nested grid. An example of our beam spacing and coverage is presented in Figures 1.1d and 1.1e. The exposure time for each pointing is 30 seconds, providing a sensitivity level that is better than 0.25 R (5σ). These approximately 30-minute blocks then form a tractable observational unit.

To avoid solar features (particularly the Hα Fronhoffer absorption line) in the background of our spectra, we only observe after astronomical twilight has ended and never observe when the moon is up. In addition, two other constrains limit when a particular block can be observed during the year. First, due primarily to the orbital velocity of the earth and the peculiar velocity of the sun with respect to the Local Standard of Rest (LSR), the velocity separation between the geocoronal Hα emission line and the zero-point of the LSR scale depends on direction in the sky and time of the year. Since most of the Galactic Hα emission occurs near 0 km s^{-1} LSR, we choose to observe blocks whose velocity separation is $\gtrsim 20$ km s^{-1} on a given night. This criteria is satisfied for every direction on some night during the year except near the ecliptic poles, where the separation is limited to a maximum of 15 km s^{-1}. With 12 km s^{-1} velocity resolution, these separations are sufficient to reliably identify the geocoronal emission and subtract it from the spectrum. The second constraint is that all observations are made above an elevation of 30° to avoid substantial atmospheric extinction corrections.

To quantify *when* is the best time to observe each block, a "score" was assigned to each block based on these two constraints. Since the velocity separation ($\Delta v_{\rm LSR}$) of the Galactic emission from the geocoronal line is more difficult to correct for than atmospheric extinction at a given zenith distance (Z), the formula

$$s = (\Delta v_{\rm LSR})^2 \times \cos Z \tag{1.1}$$

was calculated for each block in the sky for each day of the year. Then, for each block, the scores were normalized for the entire year. The resulting database was used to select the blocks with the best score (those nearest 1.0) for a given night.

1.4 Survey Operations

An actual night of observing requires about an hour of interactive setup time. Setting up WHAM consists primarily of these steps:

1. *Checking Siderostat Pointing.* Since all our observations are taken in spectral mode, we have no references in an image to confirm the coordinates of the pointing. At the start of the night, the observer switches to imaging mode and tests the pointing of the siderostat by centering on a bright star. These operations are mostly carried out by hand with the aid of two graphical tools, the CCD controller and a star finder. Both are described in §A.4.

2. *Tuning.* The pressures of the gas in the two etalon chambers need to be carefully set to "tune" the transmission peaks of the etalons to the wavelength of interest. Although the trailer where the spectrometer is kept is environmentally sealed, small ($\sim 1^\circ$ C) changes in temperature within the trailer can change the best tune from night to night. The observer points the siderostat at a bright nebula and exposures are taken at slightly different pressures to find the best tune. A graphical tool was designed to semi-automate the tuning process. Details can be found in §A.4.

3. *Planning.* Next, the observer sets up an observing script for the night. The plan consists of a list of "actions". An action is simply a bundle of lower level commands that either change the state of the spectrometer (*e.g.* switching wavelengths) or perform an observation. Observational actions take care of everything, including, pointing at the requested target, taking the exposure, and storing the data in an organized location. Entire blocks (up to 49 pointings) are organized into a single action so that the software can be extremely efficient in survey operations. For example, the siderostat is commanded to move to the next pointing in a block as the CCD is reading out the previous exposure. Since individual exposure times are 30 s, utilizing these few seconds adds up to a 10%-20% reduction in the time needed to observe a block. Planning also involves carefully selecting which blocks are optimal for a night. A tool was designed to help the observer visualize the optimal blocks (see §A.4). An example plan for the night of 1997 July 2 is presented in Figure 1.2. On this night, only Hα survey observations took place. A more complicated plan involving [S II] observations for Chapter 2 is displayed in Figure 1.3. The planning and monitoring graphical tool is described in §A.4.

Weather is monitored both by satellite images from the World Wide Web, and from a local Kitt Peak observer (Trudy Tilleman has been our primary contact) who provides the remote observer with frequent sky conditions reports via e-mail. WHAM operations are fully automated after sky observations begin. The remote observer is only needed to periodically check the night's progress for rare errors, changing weather conditions, and closing up.

1.5 Data Reduction

1.5.1 Creating Spectra

Due to the simplicity of our instrumental setup and the relatively line-free and stable skies of Kitt Peak near Hα, reduction of our spectral data is straightforward. The creation of calibrated spectra from raw WHAM images consists of these steps:

1. *Ring-Summing.* Figure 1.1a shows the raw image output from the WHAM CCD camera. This "ring image" represents the spectra from our one-degree beam. To reiterate,

unlike many other commonly used astronomical Fabry-Perot instruments, the spectral mode of WHAM records *only* spectral information—each part of the sky within the beam is sampled equally at all wavelengths and therefore no spatial information is obtained. Rings in these images are emission lines and the sharp transition at the larger radius represents the edge of our circular aperture defined by the 0.6 m diameter siderostat lens. Wavelength decreases radially from the center to the edge of the ring pattern while the azimuthal direction contains no additional information. Since we are imaging only small angles ($\theta \lesssim 2.^{\circ}09$) emerging from the etalons, $\Delta\lambda \propto v \sim \theta^2 \sim r^2$, where r is the distance of a pixel from the center of the ring image (Tufte 1997). Thus, equal-area annuli correspond to equal spectral intervals.

The image is converted into a one-dimensional spectrum by averaging the counts recorded in successive annuli. For typical WHAM data, we convert an approximately 85-pixel annulus into a spectral data point by defining a 1.96 km s^{-1} (≈ 0.043 Å at Hα) spectral window, converting to the proper range in r for the current annulus, and averaging the signal in all pixels whose centers fall within that radial range. Due to the discrete nature of the CCD pixels, these windows will not all have exactly 85 pixels, however. Currently, the velocity assigned to each window (data point) is simply an integral multiple of 1.96 km s^{-1}. The final data reduction for the survey will include a better estimate of the mean velocity of the annulus created by the discrete pixels in each window (Quigley, private communication). We employ 4×4 on-chip binning to reduce read noise. The optical setup is designed so that the last spectral ring is one 4×4 "super-pixel" wide (96 μm on the chip) and fully sampled azimuthally.

Three other smaller steps also happen at this stage:

(a) *Bias subtraction.* Bias frames are taken each night during observations. However, we have seen no significant structure in the bias images or drift in the average bias value over the three years of operation and have reduced this stage to subtracting a bias constant from each pixel in the image.

(b) *Reflection subtraction.* A 3.5% copy of the primary ring pattern is offset by $x = +37.50$, $y = -21.25$ pixels from the center of the image. This copy arises from the reflection off a wedged (0.01 rad), uncoated surface in the second etalon. To correct for this effect, the raw ring pattern is scaled, translated, and subtracted from the itself before the ring-summing takes place. Other reflections in the system are at a significantly lower level and have no detectable affect on the resulting spectra.

(c) *Cosmic ray removal.* Cosmic rays are removed in two steps. The first is a simple, three-sigma, neighbor-rejection technique that is used in many standard CCD image processing packages. We then take advantage of our azimuthal symmetry in the ring-summing to do a finer rejection. At a given radius, pixels are exposed to the same source intensity since they lie within the same spectral element. We fit a first-order polynomial to the I vs. r^2 distribution within this annulus and apply another three-sigma rejection to pixels about this line. In a typical 30 s spectra less than 1% of the image pixels are rejected with this multi-pass method.

Figure 1.1b shows the resulting ring-summed spectrum.

2. *Flat Fielding.* Our preliminary analysis shows that the majority of transmission inhomogeneities can be removed by using a white-light spectral ring image. A white-light spectrum is produced as in Step 1, and all spectra are divided by the flat field spectrum. This process removes the primary vignetting shape that causes a reduction in the transmission of order 20% from the center to the edge of the ring image with the

Hα filter. Final reduction of the WHAM survey data may also include a traditional CCD image division flat field before the ring-summing to remove pixel-to-pixel variations on the chip. However, with 85 pixels contributing to a single spectral data point, we have found that the effect of these variations is not significant, especially with our second cosmic ray step. Pixels with abnormal sensitivities are rejected with this method, improving the estimate of the original source intensity.

3. *Geocoronal Subtraction.* The primary contamination in the survey data arises from the geocoronal Hα emission line (see Figure 1.1b). This line arises primarily from excitation of neutral hydrogen in the upper layers of the earth's atmosphere by scattered solar Lyβ radiation ($n = 1 \rightarrow 3$). The subsequent decay cascade produces a prominent Hα emission feature in all sky exposures with an intensity of 2–13 R. Since the intensity of the exciting scattered Lyβ depends most sensitively on the height of the earth's shadow along the look direction, the resulting strength of the contaminating line depends on both the direction and time of the observation. For example, at a constant hour angle and declination, the intensity of this line can change by a factor of three from a minimum at midnight to a maximum at twilight. At our spectral resolution, we do not resolve the fine structure of the line and so can fit it with a single Gaussian component of width 5–8 km s^{-1}. To remove the line, we fit each individual sky spectrum and subtract the resulting geocoronal Gaussian component from the raw data. We have created a semi-automated procedure to make this correction tractable.

4. *Background Subtraction.* The brightness of the sky continuum emission at Kitt Peak within our one-degree beam at Hα is typically 30–50 ADUs (CCD counts), approximately 0.042–0.070 R (km s^{-1})$^{-1}$ or 1.9–3.2 R Å^{-1}, and is extremely flat within our 200 km s^{-1} bandpass. Stellar sources in the one-degree beam greater than fifth apparent magnitude will also noticeably elevate the background level in the spectrum. A zero- or first-order polynomial is fitted and subtracted from the raw spectrum to establish a baseline. If a bright star also has prominent absorption features (typically Hα), it can severely contaminate the spectrum. For this work, we omit these small number ($\sim 1\%$) of pointings for cosmetic reasons and average over neighboring spectra. During the cleanup phase of the survey, we will re-observe these directions with a small occulting disk near the imaging focal plane to eliminate the stellar contamination.

5. *Velocity Calibration.* Perhaps as compensation for the contamination by the geocoronal line, we gain a perfect zero-point wavelength calibrater in every spectrum. Since the geocoronal line arises primarily from ground state excitation to $n = 3$ and not from recombination, the full assembly of fine structure Hα lines are not present and the line center of the geocoronal Hα multiplet is shifted -2.3 km s^{-1} (0.05 Å) from the rest wavelength of the recombination line, 6562.82 Å. Because we carry out a fitting of this line in Step 3 above, we have a record of the line center and can establish the geocentric velocity frame. Translation from the geocentric frame to the Local Standard of Rest (LSR) is a simple calculation that depends on the direction and time of the observation. We use the same value for the Standard Solar Motion as adopted by 21 cm observers, +20 km s^{-1} toward $\alpha_{1900} = 18\overset{\text{h}}{.}0$, $\delta_{1900} = +30\overset{\circ}{.}0$.

6. *Intensity Calibration.* We observe "standard" nebular sources at least every 90 minutes. All calibrations are tied to an absolute intensity measurement of the North American Nebula (NAN; NGC 7000) within a 50′ beam at 850 R by Scherb (1981). Observations of NAN with WHAM yield the conversion: 1 R (km s^{-1})$^{-1}$ = 684 ADUs for a 30 s exposure, assuming the nebula is 800 R within our one-degree beam. However, securely tying the WHAM instrument to this reference still requires a bit more work. The data presented in this thesis also have not yet been corrected for

the effects of atmospheric extinction. The average atmospheric transmission at the zenith over our 18 months of data has been measured to be 0.92 (Babler, private communication), requiring a plane-parallel atmospheric correction of around 1.086 at 30° elevation. However, the final data reduction will include corrections for nightly differences in transmission. With this incomplete calibration and atmospheric effects yet to be accounted for, intensities quoted in this paper are good to 10%.

The results of Steps 3–6 are shown in Figure 1.1c.

7. *Fainter Atmospheric Line Subtraction.* In addition to the geocorona, several, much fainter (< 0.2 R) unidentified atmospheric lines are present near Hα in our spectra. Many of these are believed to arise from OH, which has numerous emission lines in this spectral region. Variations in the intensities of these lines are most severe from night to night and can be as large as a factor of two. Hourly variations are also seen of up to 30%. The signal-to-noise of our individual 30 s spectra do not allow accurate measurements of variability on much shorter timescales. These lines have been characterized by Hausen (private communication) and are listed in Table 1.1. Lines with widths greater than 10 km s^{-1} are most likely multiple blended lines. Most spectra presented in this thesis have not been corrected for these lines. During final survey reduction, an average spectra will be generated for each block (half-hour period) and used to derive a synthetic line spectrum that will be subtracted from each spectra of that block.

1.5.2 Assembling Maps

Once a large number of spectra are reduced, we can start to produce maps of the Galactic Hα emission. Since we are using a nested grid of pointings with little overlap of adjacent beams, we substantially reduce our time to complete the survey while still achieving near full sky coverage. However, this strategy leads to difficulties when trying to produce maps with standard display software that expects a regularly-gridded set of data. For this initial presentation, we use built-in routines provided by the IDL data reduction package to create a regularly-gridded data set from our irregularly-gridded sky pointings. In particular, we have used the TRIANULATE and TRIGRID procedures from the standard set of routines. The spacing of the output regular grid is a rather arbitrary, aesthetic parameter that can affect the appearance of discrete sources with sizes near or smaller than our beam. All the data presented here have a output grid size of $0\overset{\circ}{.}25$ to slightly oversample our input beam spacing. The resulting maps are displayed on an Aitoff projection. Figures 1.1d through 1.1f show the transition from spectra, to integrated emission, to a smoothed, regularly gridded map.

Displaying the full range of intensities is an extremely difficult problem for our data. The contrast between bright and faint regions on maps is > 100 and both the low and high intensity limits have substantial extended structure. Even logarithmic scaling does not produce satisfactory results. One possibility is to present two versions of logarithmically scaled maps, one to display structure of the bright features and one with an arbitrarily chosen upper limit to enhance the contrast in the faint regions. The problem with such a display is that we are particularly interested in the transition between bright and faint regions in our study of the WIM.

We have instead chosen to forgo the traditional arithmetic functions (linear, logarithmic, or square root) and instead use histogram equalization. This intensity scaling assigns the largest swathes of the color table to the intensities with the most pixels (or area). Color table entries are not wasted on large intensity gradients that only cover a few physical pixels. This transformation does an amazing job displaying contrast over a large range of intensity

levels, but the intensity transfer function becomes unsuitable for any reliable quantitative measurements from such maps. Since we typically supplement any maps with substantial quantitative material (*e.g.* calibrated spectra or tables of intensities), we do not view this as a loss.

Finally, we have chosen to display our maps with color instead of grayscale tables when possible. We find that color is able to highlight contrast at multiple intensities much better than grayscale. We have chosen to use a multi-color table rather than a more traditional red temperature scale since we have found that color hardcopies have a particularly hard time reproducing red gradients accurately. In all our maps, the displayed property (*e.g.* intensities or ratios) increases from blue to red.

1.6 The Hα Sky

Here we present one-third of the Hα sky, as viewed by WHAM. The map displayed in Figure 1.4 is the compilation of nearly 13,000 spectra. Total intensity ($v_{\rm LSR} = -100$ to $+100$ km s^{-1}) and three velocity intervals are shown. The curved boundary in the lower left is our -30° declination limit. Dark, single-beam sized points are contaminated by bright stars. The Galactic plane is prominently highlighted by numerous circular H II regions, while the Orion-Eridanus complex stands out as a complicated network of filaments, extending to -50° latitude. Portions of this map have been studied in previous WHAM publications including the long filament at $\ell = 225^\circ$, $b = +10^\circ$ to $+51^\circ$ (Haffner, Reynolds, & Tufte 1998; Chapter 3) and the Orion-Eridanus region (Heiles et al. 1998; Heiles, Haffner, & Reynolds 1998). The south Galactic region toward the Perseus arm is presented in Chapter 2.

In addition to providing the deepest probe of velocity-resolved features in the WIM, this new view of the Hα emission from our Galaxy can be used in a variety of ways.

- As Chapter 2 will show, regions mapped in [S II] and [N II] can be compared to the Hα emission to derive important limits on the temperature and ionization of the WIM.
- With our spectral resolution, we can also attempt to decouple the contribution of thermal and non-thermal broadening of WIM emission lines by comparing the measured line widths of Hα and S II (Reynolds 1985).
- By comparing our Hα maps to those from H I surveys we can explore the connection between the neutral an ionized phases of the ISM. Current theories for the ionization of the WIM predict a range of possibilities, from the H II and H I being completely mixed (Sciama 1990) to separated regions of ionized and neutral media (Miller & Cox 1993; Dove & Shull 1994).
- These same maps can be used to search for previously undiscovered faint, extended ionized regions around objects. Such discoveries will be important to probe for possible links between these types of regions and the pervasive background emission.
- Finally, this survey will be useful for accurately correcting for the effects of the Galactic foreground in many astrophysical observations, including, for example, corrections to Cosmic Microwave Background observations for Galactic free-free emission.

References

Dennison, B., Simonetti, J. H., & Topasna, G. A. 1998, PASA, 15, 147

Dove, J. B. & Shull, J. M. 1994, ApJ, 430, 222

Gaustad, J., McCullough, P., Van Buren, D. 1996 PASP, 108, 351

Haffner, L. M., Reynolds, R. J., & Tufte, S. L. 1998, ApJ, 501, L83

Heiles, C., Haffner, L. M., & Reynolds, R. J. 1998, New Prospectives on the Interstellar Medium, in press

Heiles, C., Reynolds, R. J., Haffner, L. M., & Tufte, S. L. 1998, in The Orion Complex Revisited, eds. M. McCaughrean & A. Burkert, in press

Miller, W. W., III, & Cox, D. P. 1993, ApJ, 417 579

Parker, Q. A. & Phillips, S. 1998, PASA, 15, 28

Percival, J. W. 1995, Proc. SPIE, 2479, 33

Percival, J. W. 1994, BAAS, 185, 6901

Reynolds, R. J. 1985, ApJ, 294, 256

Reynolds, R. J., Roesler, F. L., Scherb, F., & Harlander, J. 1990, Proc. SPIE, 1235, 610

Reynolds, R. J., Tufte, S. L., Kung, D. T., McCullough, P. R., & Heiles, C. 1995, ApJ, 448, 715

Scherb, F. 1981, ApJ, 243, 644

Sciama, D.W. 1990, ApJ, 364, 549

Tufte, S. L. 1997, PhD Thesis, University of Wisconsin–Madison

Table 1.1. Atmospheric Lines near Hα

Mean[a] (km s^{-1})	Width (km s^{-1})	Intensity (R)
+71	23.5	0.20–0.60
+40	20	0.00–0.20
−22	10	0.05–0.20
−38	10	0.10–0.30
−59	15	0.05–0.20
−83	10	0.10–0.25
−124	10	0.05–0.20

[a]With respect to the geocoronal Hα line.

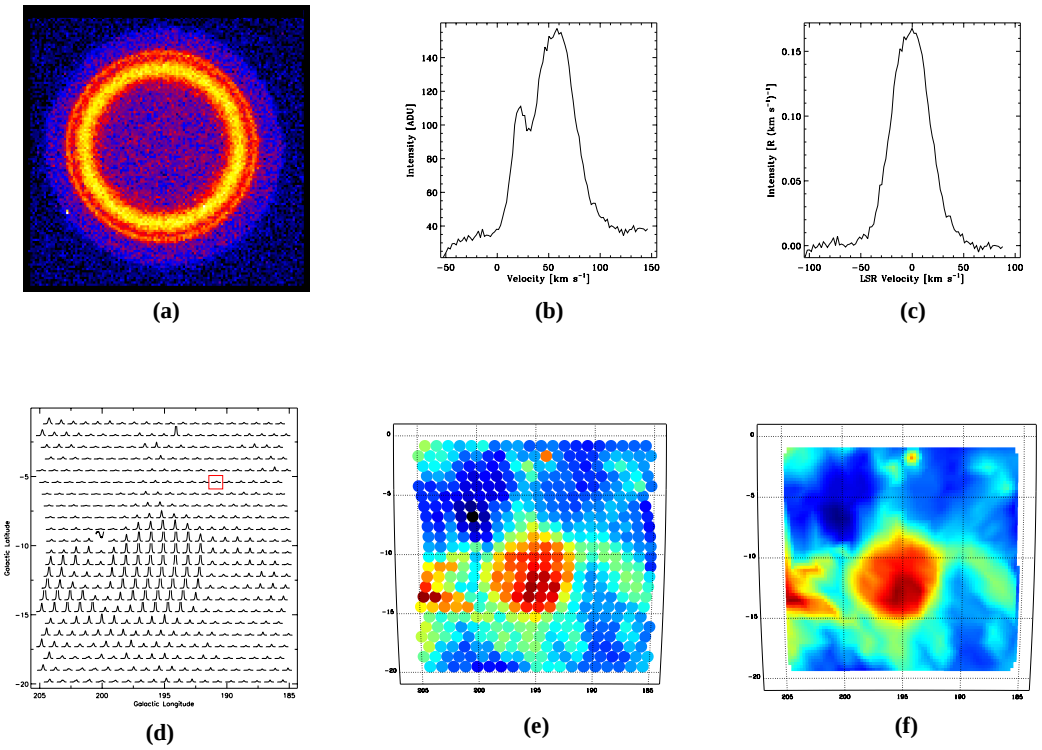


Fig. 1.1.— Steps in WHAM data reduction. (a) Raw CCD image output from WHAM in spectral mode. The sharp transition between blue (sky background) and black shows the edge of the aperture. Wavelength decreases from center to edge with a total bandpass of $\sim$ 200 km s^{-1}. The narrow, outer ring is geocoronal Hα emission. All other visible rings are formed by Galactic Hα emission. (b) Raw spectrum formed by ring summing the image in (a). The velocity scale is arbitrary. The aperture fall-off can be seen near -50 km s^{-1} while the geocoronal line appears near 20 km s^{-1}. The intensity is represented in CCD counts (ADUs). (c) Reduced spectrum after flat fielding, geocoronal and background subtraction, velocity and intensity correction. (d) Reduced spectra placed on a Galactic coordinate grid. The spectrum from (a)–(c) is outlined. (e) Colored beams representing the integrated intensity from $v_{\rm LSR} = -6$ to $+6$ km s^{-1} replace the spectra in (d). Intensities increase from blue to red. (f) A smoothed, regularly gridded version of (e). The region shown is the H II region surrounding λ Ori.

```
07/02/97 04:47:25 :: Bias
07/02/97 04:47:34 :: Bias
07/02/97 04:47:42 :: Bias
07/02/97 04:47:51 :: Calibration: Spica_HII
07/02/97 04:49:34 :: Calibration: Lockman
07/02/97 04:51:33 :: Calibration: NAN
07/02/97 04:53:11 :: Block #122
07/02/97 05:22:48 :: Block #69
07/02/97 05:51:45 :: Block #787
07/02/97 06:19:07 :: Geocorona: NCP
07/02/97 06:20:28 :: Geocorona: Z
07/02/97 06:21:51 :: Calibration: NAN
07/02/97 06:23:09 :: Block #788
07/02/97 06:52:11 :: Block #789
07/02/97 07:17:35 :: Block #835
07/02/97 07:43:50 :: Calibration: NAN
07/02/97 07:45:12 :: Block #836
07/02/97 08:12:31 :: Block #837
07/02/97 08:39:00 :: Block #838
07/02/97 09:04:57 :: Calibration: NAN
07/02/97 09:06:12 :: Geocorona: NCP
07/02/97 09:07:31 :: Geocorona: Z
07/02/97 09:08:54 :: Block #839
07/02/97 09:34:17 :: Block #840
07/02/97 10:03:51 :: Block #841
07/02/97 10:29:11 :: Calibration: NAN
07/02/97 10:30:25 :: Bias
07/02/97 10:30:35 :: Bias
07/02/97 10:30:49 :: Bias
```

Fig. 1.2.— An example of a WHAM observing plan for the night of 1997 July 2. Each line represents an single action taken by the WHAM system. Survey blocks ($\sim$ 49 pointings) are single actions to maximize observing efficiency.

```
10/11/97 08:25:25 :: Bias
10/11/97 08:25:34 :: Bias
10/11/97 08:25:42 :: Bias
10/11/97 08:25:51 :: Setup: H-Alpha (78 94.5)
10/11/97 08:27:42 :: Calibration: NAN
10/11/97 08:29:00 :: Calibration: G144_0
10/11/97 08:30:41 :: Calibration: G194_0
10/11/97 08:32:13 :: Calibration: Crab
10/11/97 08:33:33 :: Geocorona: NCP
10/11/97 08:34:38 :: Geocorona: Z
10/11/97 08:35:42 :: Setup: [S II] 6716 (141 107.5)
10/11/97 08:37:19 :: Th-Ar Calibration
10/11/97 08:38:23 :: Ne Calibration
10/11/97 08:38:59 :: Calibration: NAN
10/11/97 08:41:00 :: Calibration: G144_0
10/11/97 08:42:40 :: Calibration: G194_0
10/11/97 08:44:12 :: Calibration: Crab
10/11/97 08:45:33 :: Geocorona: NCP
10/11/97 08:46:41 :: Block #848
10/11/97 09:36:43 :: Calibration: G144_0
10/11/97 09:38:08 :: Calibration: G194_0
10/11/97 09:39:38 :: Block #849
10/11/97 10:27:36 :: Calibration: G144_0
10/11/97 10:29:00 :: Calibration: G194_0
10/11/97 10:30:30 :: Block #692
10/11/97 11:23:54 :: Calibration: G144_0
10/11/97 11:25:11 :: Calibration: G194_0
10/11/97 11:26:40 :: Calibration: Crab
10/11/97 11:28:00 :: Calibration: Lockman
10/11/97 11:30:35 :: Geocorona: NCP
10/11/97 11:31:38 :: Setup: H-Alpha (78 94.5)
10/11/97 11:33:30 :: Calibration: G144_0
10/11/97 11:34:57 :: Calibration: G194_0
10/11/97 11:36:26 :: Calibration: Crab
10/11/97 11:37:45 :: Calibration: Lockman
10/11/97 11:39:18 :: Geocorona: NCP
10/11/97 11:40:20 :: Geocorona: Z
10/11/97 11:41:29 :: Block #448
10/11/97 12:00:25 :: Calibration: G144_0
10/11/97 12:01:35 :: Calibration: Crab
10/11/97 12:02:33 :: Calibration: G194_0
10/11/97 12:03:22 :: Calibration: Lockman
10/11/97 12:04:58 :: Bias
10/11/97 12:05:12 :: Bias
10/11/97 12:05:35 :: Bias
```

Fig. 1.3.— An example of a WHAM observing plan for the night of 1997 October 11. Observations of [S II] used in Chapter 2 involve more changes in the spectrometer. Since our primary calibration source, NAN, is not available for the whole night, several secondary calibrators are observed after each hour-long [S II] block.

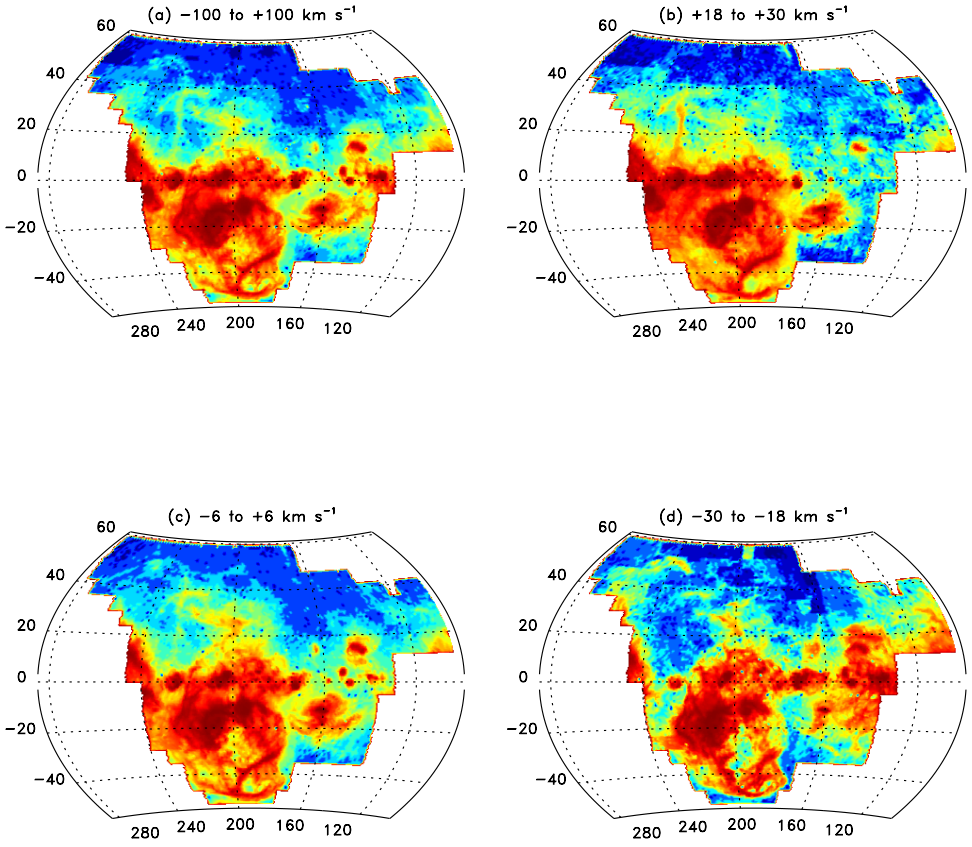


Fig. 1.4.— A sample (about a third) of the WHAM Hα All Sky Survey. Pseudo-color represents integrated Hα intensity within the labeled velocity band. Axes are Galactic longitude and latitude. Small, dark points are beams contaminated by stars that have not yet been corrected. The dynamic range for each panel is different.

Chapter 2

WHAM observations of Hα, [S II], and [N II] toward the Orion and Perseus Arms: Probing the Physical Conditions of the WIM

Abstract

A large portion of the Galaxy ($\ell = 123°$ to $164°$, $b = -6°$ to $-35°$), which samples regions of the Local (Orion) spiral arm and the more distant Perseus arm, has been mapped with the Wisconsin H-Alpha Mapper (WHAM) in the [S II] λ6716 and [N II] λ6583 lines. By comparing these data with the maps from the WHAM Hα Sky Survey, we begin an investigation of the global physical properties of the Warm Ionized Medium (WIM) in the Galaxy. Several trends noticed in emission-line investigations of diffuse gas in other galaxies are confirmed in the Milky Way and extended to much fainter gas. In particular, we find that the [S II]/Hα and [N II]/Hα ratios increase as absolute Hα intensities decrease. Examining only the more distant Perseus arm emission, we find that the increase in these ratios is a strong function of Galactic latitude, b, and thus, of height, z, above the Galactic plane. We also find that the [S II]/[N II] ratio is relatively independent of Hα intensity. Scatter in this ratio appears to be physically significant, and maps of [S II]/[N II] suggest regions with similar ratios are spatially correlated. The Perseus arm [S II]/[N II] ratio is systematically lower than Local emission by 10%–20%. With [S II]/[N II] constant over a large range of Hα intensities, a possible explanation of [S II]/Hα and [N II]/Hα trends is that they are primarily due to changes in temperature. Such an interpretation allows us to estimate the temperature and ionization conditions in our large sample of observations. We find that WIM temperatures range from 6,000 K to 9,000 K with temperature increasing from bright to faint Hα emission (low to high [S II]/Hα and [N II]/Hα) respectively. Changes in [S II]/[N II] appear to reflect changes in the local ionization conditions (*e.g.* the S^+/S^{++} ratio). We also confirm earlier measurements of the electron scale height in the Perseus arm to be $H = 1.0 \pm 0.1$ kpc. Finally, we explore a newly discovered H II region centered near $\ell = 131°$, $b = -11°$, most likely excited by the ϕ Per system. We calculate that the Lyman continuum flux needed to sustain the nebula is 1.0×10^{47} ph s^{-1}.

2.1 Introduction

Although the WHAM Hα Sky Survey will present the first view of the distribution and kinematics of the WIM component, we still know little about the physical conditions in this gas or how they are produced. Several studies have measured constraints on important parameters toward specific regions of the WIM, but none has yet provided a large sample of measurements to help test how environmental conditions (*e.g.* distance from H II regions, distance from the Galactic plane, etc.) might affect these physical conditions.

Reynolds (1985a) derived the first estimate of the temperature of the WIM by combining measured line widths of [S II] and Hα emission toward the same regions. He was able to place limits between 5,000 K and 20,000 K, with a mean of about 8,000 K, on the temperature of a sample of 21 WIM observations. Ionization conditions have been probed even less, with most of our current information coming from observations in the plane of the Galaxy. Reynolds (1985b) showed that [O III] λ5007 emission is very faint in the WIM, placing limits on the amount of O^{++} (needing $E > 35.1$ eV) in the WIM. More conclusively, Reynolds & Tufte (1995) and Tufte (1997) have shown via observations of the He I λ5876 line that the fraction of He^{+} (needing $E > 24.6$ eV) in this gas is also quite low in comparison with traditional O star H II regions. In addition to these limits on the higher energy portion of the ionizing spectrum is the recent detection of [O I] λ6300 from three WIM directions (Reynolds, et al. 1998). The low [O I]/Hα ratios seen in all of these directions suggests that the H is mostly H^{+} in the Hα emitting gas.

The advent of WHAM provides a unique opportunity to trace some of these diagnostics over a larger region of the sky. This chapter presents the first velocity-resolved study of [S II] and [N II] from the diffuse gas of our Galaxy. A region of the sky that includes the Perseus arm was chosen for examination since the Hα emission from the WIM in this arm is well separated from local WIM emission and can be traced to high Galactic latitude, allowing an exploration of the emission with distance, z, from the Galactic plane. Such observations can be directly compared to studies of edge-on galaxies, most notably those by Rand (1997, 1998) on NGC 891. The primary trends found in his work are borne out here and extended to even fainter emission measures. Specifically, [S II]/Hα and [N II]/Hα ratios increase with $|z|$, while [S II]/[N II] ratios remain nearly constant.

2.2 Observations

The Hα observations of the 1000 deg^2 region $\ell = 123^\circ$ to 164°, $b = -6^\circ$ to -35° that is the focus of this study were obtained between 1997 July and 1997 October as a part of the WHAM Hα Sky Survey (cf. Chapter 1). Additional observations at the same survey grid points but with the 200 km s^{-1} spectral window tuned near the [S II] λ6716 and [N II] λ6583 line were obtained in 1997 October, 1997 November, and 1998 June. The region presented here is sampled by 1360 Hα, 1360 [S II], and 1360 [N II] spectra, each representing the integrated emission within WHAM's one-degree beam. The integration times for each spectrum was 30 s for Hα and 60 s for the other two emission lines.

The [S II] and [N II] observations are converted into spectra using the same steps as those for Hα presented in §1.5.1. Separate white-light flat fields were created for each of these additional filters and used in place of the Hα flat field. Since there appears to be no strong terrestrial component in [S II] or [N II], Step 3 is skipped. For the [S II] observations, the weak terrestrial (Tucson lights) Ne I line at 6717.04 Å is used for velocity calibration. For the [N II] observations, spectra of Hα and [N II] from bright emission nebulae were compared and the velocity frame of [N II] was adjusted so that the mean velocity of the nebular [N II] emission matches that of the Hα. Intensities were calibrated in Step 6 by

applying a correction factor to the [S II] and [N II] observations (0.94 and 1.15, respectively) based on the transmission differences between these filters and Hα.

As in the Hα observations, the [S II] and [N II] spectra are contaminated by weak, atmospheric lines (cf. §1.5.1). The brightest of these in our [S II] spectra is the Ne I line located +26.8 km s^{-1} from the geocentric zero of [S II] λ6716. As noted above, it proves to be a useful wavelength calibrator. To accurately characterize the parameters of these faint lines, we created an average spectrum for each observational block ($\approx$ 49 pointings). Following the strategy outlined in Step 7 of the Hα data reduction in Chapter 1, a single Gaussian was fitted to each of the lines and subtracted from the individual pointings. These corrections account for hourly variations in these faint lines. A list of the atmospheric lines in our [S II] and [N II] observations is given in Table 2.1. The potential line at -40 km s^{-1} in [N II] is coincident with Perseus arm emission in all spectra presented here. The implications of such a line are discussed in §2.4.1.

2.3 Results

2.3.1 Overview

Figure 2.1a displays the integrated Hα intensity for our selected region. The box overplotted in the image denotes the $10^\circ \times 12^\circ$ region previously mapped in Hα by Reynolds (1980) and compared to H I observations in detail by Reynolds, et al. (1995). The remaining panels of Figure 2.1 represent integrated, 12 km s^{-1} wide velocity slices. The [S II] and [N II] maps look qualitatively similar to Hα and are not reproduced here. Figure 2.2 shows samples of Hα spectra from this region of the Galaxy. The Local (0 km s^{-1}) and Perseus arm (-40 to -60 km s^{-1}) emission are clearly shown as well-separated components in the right-hand panels where $\ell < 150^\circ$.

Two large Hα emitting regions dominate the integrated emission at lower latitudes, above $b = -20^\circ$. The brightest emission arises from NGC 1499 (California Nebula) excited by the O7.5I star ξ Per located 543 $^{+334}_{-149}$ pc away (*Hipparcos*; Perryman 1997). Emission in the nebula itself, a $5^\circ \times 2^\circ$ crescent centered near $\ell = 160^\circ$, $b = -13^\circ$, peaks at over 250 R (1 R = $10^6/4\pi$ ph cm^{-2} s^{-1} sr^{-1} = 2.4×10^{-7} erg cm^{-2} s^{-1} sr^{-1} at Hα) and is centered around $v_{\rm LSR} = -5$ km s^{-1}, while faint, extended emission above 5 R centered near $v_{\rm LSR} = +5$ km s^{-1} continues 5–7° away from the nebula. This extended H II region has been studied in some detail by Reynolds (1988), who first hypothesized that the bar of emission ($I_{\rm H\alpha} \approx 8$ R) running from $\ell = 150^\circ$, $b = -20^\circ$ to $\ell = 142^\circ$, $b = -10^\circ$ centered between $v_{\rm LSR} = -5$ to $+5$ km s^{-1} may also be ionized by the star. The second large emission region, centered near $\ell = 131^\circ$, $b = -11^\circ$, is a superposition of separate, but equally bright emission regions in the Local and Perseus arms (see Figure 2.2). Emission from the Local arm is near $v_{\rm LSR} = 0$ km s^{-1} and has a more circular appearance reminiscent of a classical Strömgren sphere (see Figure 2.1b). This faint H II region has a relatively constant brightness of 5–6 R over most of its 13° diameter area. We discuss the region in detail in §2.4.2 below. Emission from the Perseus arm in this direction at $-60 < v_{\rm LSR} < -40$ is more much more amorphous in shape (*e.g.* Figure 2.1f).

At higher latitudes and at velocities farther from the LSR, the Hα emission becomes quite filamentary. Some of the more notable structures include a faint bar in Figure 2.1e running from $\ell = 150^\circ$, $b = -33^\circ$ to $\ell = 160^\circ$, $b = -25^\circ$; several, nearly vertical filaments in Figure 2.1f near $\ell = 130^\circ$, $b = -20^\circ$; and the shell-like region and associated dissecting filament in Figure 2.1h. The last of these was previously studied in detail by Ogden & Reynolds (1985) and Reynolds et al. (1995).

2.3.2 Scale Height of the WIM

Since the Perseus arm gas is well separated in velocity from the Local emission, we can explore the decrease of this emission as a function of the height above the Galactic plane. To extract information about the scale height from the intensity distribution, we first assume that the gas density is primarily a function of z and has the form

$$n_e(z) = n_e^0 \; e^{-|z|/H} \; \mathrm{cm}^{-3}, \tag{2.1}$$

where n_e^0 is the mid-plane density and H is the scale-hight of the WIM. The Hα intensity is related to the gas density by the equation

$$2.75 \; T_4^{0.9} \, I_{\mathrm{H}\alpha} = \int n_e^2 \; \phi \; dl, \tag{2.2}$$

where ϕ is the filling fraction of the emitting gas, T_4 is the temperature of the gas in 10^4 K, and $I_{\mathrm{H}\alpha}$ is in R. As long as the temperature, filling factor, and pathlength through the emitting gas, $\int dl = L$, are not functions of z we then have

$$I_{\mathrm{H}\alpha} = \frac{(n_e^0)^2 \, \phi \, L}{2.75 \, T_4^{0.9}} \; e^{-2|z|/H} = I_{\mathrm{H}\alpha}^0 \; e^{-2|z|/H}, \tag{2.3}$$

where $I_{\mathrm{H}\alpha}^0$ is the intensity at the mid-plane. Finally, substituting $z = D \, \tan|b|$, where D is the distance to the arm and b is the Galactic latitude of an observation, and taking the natural log, we arrive at

$$\ln I_{\mathrm{H}\alpha} = \ln I_{\mathrm{H}\alpha}^0 - \frac{2D}{H} \tan|b|. \tag{2.4}$$

Figure 2.3 plots this relationship for a selected region of the map. Each point represents the median emission between $\ell = 125°$ and $152°$. The median of the emission in each latitude slice is used instead of an average to reduce the effect of local emission enhancements (*e.g.* faint H II regions). The limited longitude range is chosen to avoid the gradual blending of the Perseus arm component with the Local gas as the longitude approaches $180°$. Three radial velocity intervals are presented in the plot, reflecting total ($v_{\mathrm{LSR}} = -100$ to $+100$ km s^{-1}), Local ($v_{\mathrm{LSR}} = -25$ to $+100$ km s^{-1}), and Perseus arm ($v_{\mathrm{LSR}} = -100$ to -25 km s^{-1}) emission. The error bars for the Perseus arm are an estimate of the measurement error calculated from the average deviation about the median of emission within a latitude slice.

Also displayed in Figure 2.3 is a linear fit to Perseus arm points that are above $b = -15°$. Closer to the plane, H II regions and extinction play a significant role and these points are excluded from the fit. The resulting fit parameters are $\ln I_{\mathrm{H}\alpha}^0 = 1.73 \pm 0.19$ and $2D/H = 4.91 \pm 0.39$, leading to a mid-plane intensity for the WIM of 5.7 ± 0.2 R and a scale height of 1.0 ± 0.1 kpc if the Perseus arm is near 2.5 kpc (see Reynolds et al. 1995 and references therein). The dotted line in Figure 2.3 presents a manual fit to the lower envelope of the Perseus arm emission. The resulting parameters are essentially the same: $H = 1.0$ kpc and $I_{\mathrm{H}\alpha}^0 = 4.2$ R. The 1.0 kpc scale height appears to be valid for $|z|$ from 750 pc to at least 1700 pc, the boundary of this studied region. This estimate assumes the filling fraction, ϕ, does not depend on $|z|$. If in fact ϕ changes as a function of height above the plane, it affects our estimate of the electron scale height. In particular, if ϕ increases with $|z|$ as suggested by Kulkarni & Heiles (1987) and Reynolds (1991), our estimate of the scale height is too low.

2.3.3 Line Ratios

Figures 2.4 and 2.5 present pseudo-color images of (a) [N II]/Hα and (b) [S II]/[N II] line ratios integrated over $v_{\rm LSR} = -10$ to $+10$ km s^{-1} (Figure 2.4) and $v_{\rm LSR} = -30$ to -50 km s^{-1} (Figure 2.5), sampling the Local and Perseus arms, respectively. The [S II]/Hα maps are similar to those of [N II]/Hα, but have less contrast, and are not shown here. The [N II]/Hα maps generally anti-correlate with Hα maps except for the H II region centered near $\ell = 131°$, $b = -11°$ discussed in §2.4.2 below. [S II]/[N II] ratios are also generally lower in brighter Hα regions, which in this region are dominated by the two H II regions.

In Figures 2.6 and 2.7, [S II]/Hα and [N II]/Hα are plotted against Hα intensity. The integration ranges for each panel of the figures are restricted to separate the Local and Perseus arm emission. As above, the longitudinal extent of the Perseus observations is limited to $\ell < 152°$. We denote the pointings within the newly discovered Local arm H II region (see §2.4.2) with a square symbol. Note that these points appear to form the upper envelope of the [S II]/Hα ratios for their Hα intensities (Figure 2.6) and actually form a distinctly different horizontal branch in the [N II]/Hα ratios (Figure 2.7). In general, both figures show a marked increase in these ratios with decreasing Hα intensity. For comparison to a more traditional H II region in this mapped area, the horizontal, solid line at the right edge of both figures shows the average ratio from the six pointings with $I_{\rm H\alpha} > 50$ R near NGC 1499: [S II]/Hα = 0.14 and [N II]/Hα = 0.39. Ratios for a brighter H II region, our calibration source NGC 7000 ($I_{\rm H\alpha} = 800$ R), are [S II]/Hα = 0.06 and [N II]/Hα = 0.20 (see also Reynolds 1985a).

Figure 2.8 plots these two line ratios against one another. In both the Local and Perseus arms, the ratios appear to be strongly correlated. In this figure, both the ϕ Per and ξ Per H II regions are highlighted with square and triangle symbols, respectively. Both appear to occupy specific loci in such a plot that are different not only from one another, but from the general WIM background. The Perseus arm panel is again restricted to $\ell < 152°$.

As discussed in §2.3.2, the general trend in Hα intensity is that it decreases as the observed gas lies farther from the Galactic plane. Figures 2.9 and 2.10 show that the relationship of the [S II] and [N II] to Hα ratios versus Hα intensity described above translate directly into an increase of these ratios with increasing $|b|$ and, for the Perseus arm, $|z|$. The top panel of each figure shows all three emission lines using the same axes as Figure 2.3. The bottom panel shows the three line ratios [N II]/Hα, [S II]/Hα, and [N II]/[S II]. Both figures are restricted to the longitude range $\ell = 125°$–$152°$ for consistency. The [N II]/[S II] ratio is relatively constant, with perhaps a slight increase in the Local arm and decrease in the Perseus arm with increasing $|b|$.

2.4 Discussion

2.4.1 Physical Parameters of the WIM

The tight correlation of [S II] and [N II] emission in Figure 2.8 results in a fairly constant value of [S II]/[N II] over a wide variety of Hα intensities and latitudes. This result has been seen in numerous studies of the extragalactic WIM analogue, commonly referred to as the diffuse ionized gas (DIG) (Rand 1998; Wang, Heckman, & Lehnert 1997; Greenawalt, Walterbos, & Braun 1997). As Rand covers in detail, current photoionization models (*e.g.* Domgörgen & Mathis 1994; Sokolowski 1994) have difficulty keeping this ratio constant as [S II]/Hα and [N II]/Hα rise. Abundance gradients and H II region contamination can be a larger problem in interpreting such ratios in extragalactic studies with the large physical sizes represented by a typical data point. Our new observations within the Galaxy provide smaller scales and adequate velocity resolution to separate radial components of gas, avoiding some of these problems.

We suggest that the correlation seen in our data arises simply from the dominance of S^+ and N^+ ionization states in this gas together with the similar excitation potential of these two emission lines. With this idea, we attempt to derive estimates of the electron temperature and ionization state of S within our sample. We start with the basic equation for the intensity of emission lines from collisionally excited ions (Osterbrock 1989),

$$I_\nu \ (\mathrm{ph\ s^{-1}\ cm^{-2}\ ster^{-1}}) = \frac{f_\nu}{4\pi} \int n_i\, n_e\, \frac{8.63\times10^{-6}}{T^{0.5}}\, \frac{\Omega(1,2)}{\omega_1}\, e^{-\frac{hc}{\lambda kT}}\, dl, \tag{2.5}$$

where $\Omega(1,2)$ is the collision strength of the transition, ω_1 is the statistical weight of the ground level, λ is the wavelength of the transition, and f_ν is the fraction of collisional excitations that produce the emission line in question. We adopt values of the collision strengths Ω from Osterbrock (1989) so that $\Omega_{[\mathrm{N\ II}]\,6583} = 2.68$ and $\Omega_{[\mathrm{S\ II}]\,6716} = 4.19$. A term to account for extinction has not been included here, since the three lines we are considering are close in wavelength.

To arrive at any estimates, we must be able to compute the path averaged integrals in these equations. Since there is little knowledge yet of the details of the spatial distribution of the physical parameters in the WIM, we take the simplest approach and assume that physical values do not vary along a path. For the ratios we calculate below, we need to make this assumption for the temperature, ionization, and abundance of the gas. Our estimates should then be viewed as representative values, rather than accurately reflecting local conditions from where the emission arises. Since we are able to cleanly separate Local and Perseus arm gas, large-scale Galactic variations can be probed along lines of sight, even with this assumption. This simplification also implies that the line emission from the three ions originates from the same location. This is probably a valid assumption in the WIM, unless local processes on small scales (*e.g.* shocks) dominate the ionization structure. In H II regions, however, this assumption most likely breaks down since the ionization structure of the nebula could be changing significantly within our beam.

With this simplification, we arrive at these two equations for the intensity of [S II] and [N II] emission,

$$I_{6716}\ (\mathrm{R}) = 2.79\times10^5 \left(\frac{H^+}{H}\right)^{-1} \left(\frac{S}{H}\right) \left(\frac{S^+}{S}\right)\ T_4^{-0.5}\, e^{-2.14/T_4}\, EM, \tag{2.6}$$

and

$$I_{6583}\ (\mathrm{R}) = 5.95\times10^4 \left(\frac{H^+}{H}\right)^{-1} \left(\frac{N}{H}\right) \left(\frac{N^+}{N}\right)\ T_4^{-0.5}\, e^{-2.18/T_4}\, EM \tag{2.7}$$

where T_4 is in units of 10^4 K and $EM = \int n_e^2\, dl$ is the emission measure in units of $\mathrm{cm^{-6}}$ pc. Note also that I is now in R ($1\ \mathrm{R} = 10^6/4\pi$ ph $\mathrm{cm^{-2}\ s^{-1}\ sr^{-1}} = 2.4\times10^{-7}$ erg $\mathrm{cm^{-2}\ s^{-1}\ sr^{-1}}$ at Hα). The [S II]/[N II] intensity ratio is then

$$\frac{I_{6716}}{I_{6583}} = 4.69\, \frac{\left(\frac{S}{H}\right)}{\left(\frac{N}{H}\right)}\, \frac{\left(\frac{S^+}{S}\right)}{\left(\frac{N^+}{N}\right)}\, e^{0.04/T_4}. \tag{2.8}$$

We use the solar $(\mathrm{S/H}) = 1.86\times10^{-5}$ from Anders & Grevesse (1989) and $(\mathrm{N/H}) = 7.5\times10^{-5}$ from Meyer, Cardelli, & Sofia (1997) for the gas-phase abundances of S and N.

Because N and H have similar first ionization potentials (14.5 and 13.6 eV) and a weak charge-exchange reaction, N^+/N^0 tracks H^+/H^0 in photoionization models (Sokolowski 1994), so that in Hα emitting regions, where the fractional ionization of H has been measured to be near unity (Reynolds et al. 1998), $N^+/N \to 1$ also. Sulfur has a low enough first ionization potential, 10.4 eV, that it is most likely fully ionized in the gas we are studying.

In addition, its second potential, 23.4 eV, lies slightly below the neutral He edge at 24.6 eV, and therefore, it is likely that both S^+ and S^{++} are present in WIM gas (see also Howk & Savage 1999). Nitrogen, on the other hand, with a second ionization potential of 29.6 eV, most likely ionizes no higher than N^+. Recent photoionization models run by Howk & Savage (1999) over a wide range of temperatures and ionization parameters show that even if the ionizing spectrum in the WIM is as hard as $T_e \approx 40,000$ K, $S^{++}/S < 0.5$ and $N^{++}/N < 0.3$. Furthermore, Reynolds & Tufte (1995) and Tufte (1997) found that He^+/He ranges from 0.3 to about 0.6 in the WIM, suggesting that indeed some S will be ionized to S^{++}.

In the limit where S^+/S and N^+/N are both unity and at a typical WIM temperature of $T_4 = 0.8$ K, Equation 2.8 gives $I_{6716}/I_{6583} = 1.22$. This relationship is plotted as the solid line in Figure 2.11. Dotted lines of lower slope show the effect of decreasing S^+/S (presumably due to an increase in S^{++}) while keeping $N^+/N = 1$. In this interpretation, the data imply that S^+/S ranges between about 0.25 and 0.8, with an average value for the Local diffuse background of 0.6–0.65. Furthermore, the location of the H II region symbols in Figure 2.11 indicate that these regions have systematically lower S^+/S than the diffuse background. This is probably due to the fact that closer to the ionizing source, S^+ is ionized to S^{++}, producing a corresponding decrease in the observed [S II] intensity.

Just as the [N II]/Hα and [S II]/Hα ratios can give us information on the ionization state of S, the ratios can provide some estimate of the temperature. From Equations 2.2 and 2.7 the [N II]/Hα ratio is given by

$$\frac{I_{6583}}{I_{\mathrm{H}\alpha}} = 1.63 \times 10^5 \left(\frac{H^+}{H}\right)^{-1} \left(\frac{N}{H}\right) \left(\frac{N^+}{N}\right) T_4^{0.4}\, e^{-2.18/T_4}. \tag{2.9}$$

Since $N^+/N \approx H^+/H$ (see above), the H and N ionization factors can be removed from Equation 2.9. As an example, the typical WIM temperature of $T_4 = 0.8$ then leads to [N II]/Hα = 0.73. Lines of constant temperature are plotted on Figure 2.11 as dashed vertical lines. With a better estimate for temperature, we also recompute Equation 2.8 to form the dash-dotted line in Figure 2.11. This correction is small.

Figure 2.12 shows the same grid of S^+/S and T overplotted on the Perseus arm ratios. The limits placed on S^{++}/S in the WIM by Howk & Savage (1999) are at odds with the significant number of points below the $S^+/S = 0.5$ line in the Perseus arm. As noted in §2.2, there may be an atmospheric line within the integration range of Perseus arm emission. By comparing [S II] and [N II] spectra toward the same locations, we derive an upper limit of 0.1 R for the intensity of this line. The effect of removing this line is displayed in Figure 2.12 for the sample error bar points by the dotted line and dotted error cross. Such a correction would imply a slightly higher S^+/S ratio on average for the Perseus arm, but not enough to explain the entire difference between the arms. We may be probing a harder radiation field in the Perseus arm gas than their model input spectra or, our assumed value of S/H may be too high. A reduction in the sulfur abundance by 0.5–0.75 (0.3–0.1 dex) would bring our inferred S^{++}/S fractions more in line with their models.

The Perseus arm gas appears to have systematically lower S^+/S than the Local arm, with an average value closer to 0.5. Equation 2.8 shows that differences in abundances between the Local and Perseus arm could change the slope of the [S II]/Hα and [N II]/Hα relationship. However, Afflerbach, Churchwell, & Werner (1997) measured the Galactic abundance gradients in ultra-compact H II regions for O, S, and N. Using their best fits, N/H falls off faster than S/H with increasing Galactocentric distance so that S/N is $\sim 5\%$ higher in the Perseus arm. This is the opposite effect needed to explain the difference in the Perseus and Local arm emission ratios.

More likely, Figure 2.12 suggests that this region of the Perseus arm has a higher fraction of S^{++} than the Local arm region. Rand (1998) observed an increase in [O III]/Hβ

with height above the plane of NGC 891 and concluded that an additional source of ionization is needed beyond photoionization from hot stars in the disk. In a region where O^{++} ions are being maintained, S^+ becomes a less dominant species. This is consistent with the inferred differences in S^+/S between the Perseus arm (Figure 2.12) and Local arm (Figure 2.11) data, since lines of sight pass through the Perseus arm at much higher $|z|$ than for Local gas. One problem with this interpretation is that we do not see a substantial fall in the [S II]/[N II] ratio with increasing $|z|$ in the Perseus arm (Figure 2.10). Instead of an additional ionizing source, it is also possible that there are marked differences in the strength of the halo ionizing field between the Local and Perseus arms. For example, NGC 891 shows considerable variation in the extent of extended Hα emission along the galactic plane (Rand, Kulkarni, & Hester 1990; Rand 1998).

The scatter of data points suggests significant variations in the electron temperature within the mapped region, from about 6,000 K to 10,000 K. The most striking result from these temperature estimates comes when re-examining the [N II]/Hα ratio in Figures 2.5a and 2.10. From the rise in this ratio with increasing $|z|$, we infer that the temperature in the halo rises from about 7,000 K at $|z| = 0.75$ kpc ($b \sim -17^\circ$) to over 10,000 K at $|z| = 1.75$ kpc ($b \sim -35^\circ$). Note also that since fainter regions tend to have higher [N II]/Hα (Figure 2.7), our analysis implies that fainter regions are hotter. Since $EM \propto I_{\mathrm{H}\alpha} T^{0.9}$, higher temperature regions naturally produce lower Hα intensities; however, even after applying this temperature correction to $I_{\mathrm{H}\alpha}$, regions with lower EM are still hotter. Since EM depends only on n_e^2 and the pathlength through the emitting region, one of the two must be smaller in these fainter, hotter regions. Pathlength is an inherently unphysical parameter to link to temperature and we can think of no reason why our data set would bias shorter pathlength sightlines toward higher temperature regions. Thus, we conclude that the hotter regions most likely have smaller $\langle n_e^2 \rangle$. Since n_e in our mapped region of the Perseus arm decreases with increasing $|z|$ (see §2.3.2), we are not able to ascertain from these data whether n_e or $|z|$ is the fundamental parameter influencing the electron temperature.

Note that if the electron temperature is truly rising with $|z|$ as our results suggest, the calculation of the scale height of Hα emitting gas (§2.3.2) becomes more complicated. If we confirm this effect with future observations (see §2.5), the net effect (Equation 2.2) is that the true scale height of the gas is larger than the value calculated in §2.3.2).

2.4.2 A Faint, Diffuse H II Region

As Figure 2.1b shows, there is a nearly circular region of emission 13° in diameter centered near $\ell = 131^\circ$, $b = -11^\circ$. The region also stands out clearly in the Local arm line ratios in Figure 2.4a and b. Figure 2.13 displays latitude and longitude emission-line cuts through the apparent center of the region. Emission line ratios are plotted as dotted lines. The latitude cut also crosses the upper portion of the ξ Per H II region at longitudes $> 150^\circ$. The most promising candidate for an ionizing source for this region is ϕ Per, a B0.5e + sdO binary system located at $\ell = 131.^\circ 3$, $b = -11.^\circ 3$ and $220\ ^{+43}_{-32}$ pc away (*Hipparcos*; Perryman 1997). At that distance, the region is 50 pc in diameter.

A few important facts can be drawn from Figure 2.13. First, the [S II] and [N II] to Hα ratios in this H II region are significantly different than the brighter ξ Per region (see also Figure 2.8). While the ξ Per (O7.5I) region has low values of these ratios typical of those inside bright H II regions (Reynolds 1985a), the line ratios in the fainter H II region are closer to the WIM ratios seen at more negative latitudes in the longitude cut. Second, the cuts in ℓ and b suggest that these ratios actually *rise* near the edge of the H II region—above even WIM gas ratios. Both these points are highlighted in Figure 2.4a, which shows a map of the [N II]/Hα ratio.

The circular shape of the region in Figure 2.1b also suggests that it is a sphere of uniform emissivity. To compare the emission profile of a perfectly spherical, constant-density

region to this newly discovered region, we construct synthetic Hα intensity profiles in ℓ and b. From Equation 2.2,

$$I_{\mathrm{H}\alpha} \propto \mathrm{EM} = \int n_e^2 \, dl, \tag{2.10}$$

which is directly proportional to the pathlength through the emitting region ($\int dl = L$) if n_e is constant. The pathlength though a sphere is simply a function of the impact parameter, r, of a particular sightline:

$$L = 2\mathcal{R}\sqrt{1-(r/\mathcal{R})^2} \tag{2.11}$$

Here $\mathcal{R}$ is the maximum radius of the region, $220 \tan 6.5^\circ = 25$ pc, and $r = 220 \tan\theta$, where θ is the angular distance of the sightline from the center of the H II region. The resulting profile is plotted on both panels of Figure 2.13 as a dashed line and match the real emission in both cuts quite well. The peak of the synthetic profile is scaled to the peak of the real emission and the profile has been added to the WIM background measured outside the region.

A spherical H II region is most easily explained by exhausting the Lyman continuum (LyC) photons produced by the central source. Thus, by measuring the total Hα flux from the region, we can estimate the LyC luminosity, L_c, needed to sustain the emission from the relation

$$L_c = \frac{4\pi d^2}{\epsilon} \int I_{\mathrm{H}\alpha} \, e^{\tau_\alpha} \, d\Omega, \tag{2.12}$$

where d is the distance to the region, $I_{\mathrm{H}\alpha}$ is the Hα intensity emitted by the solid angle $d\Omega$, ϵ is the fraction of Hα photons produced per Lyman continuum photon (0.47 at 8000 K; Martin 1988; Reynolds 1971), and e^{τ_α} is the extinction correction factor. The detection of this region therefore provides a rare opportunity to measure the LyC luminosity of a B star.

For our observations, which are composed of N pointings within the area of the H II region, Equation 2.12 can be rewritten as

$$L_c = 2.03 \times 10^{43} \, d^2 \, (\frac{\Omega_{\mathrm{HII}}}{N\Omega_p}) \sum_N I_{\mathrm{H}\alpha} \, e^{\tau_\alpha} \, \Omega_p, \tag{2.13}$$

where, Ω_p is the solid angle subtended by a single pointing of the 1° beam, 2.39×10^{-4} ster, while the ratio $\Omega_{\mathrm{HII}}/N\Omega_p$ corrects for the gaps and overlaps of the survey grid within the H II region. For this region the ratio is 1.06 with our beam spacing. Also, d is in pc, $I_{\mathrm{H}\alpha}$ is in R, and L_c is ph s^{-1}.

All pointings within 6.5° of the center of the H II region ($\ell = 131^\circ$, $b = -11^\circ$) are used for this computation. Each spectrum within this radius is numerically integrated from $v_{\mathrm{LSR}} = -20$ to $+100$ km s^{-1}. The negative velocity cutoff is imposed to avoid adding a significant amount of Perseus arm emission to the calculation. To see if this cutoff significantly reduces our Local emission calculation, we compare full Gaussian component fits to the result of numerical integration for several pointings. As a result, an additional 3% is added to the area computed by numerical integration to more accurately reflect the total emission from the Local component. Finally, 1.2 R is subtracted from each pointing to account for the contribution of Local WIM gas to the total observed emission in that direction. We make this estimate by examining the Hα emission in the regions adjacent to the H II region. Since the H II region emission is 2–3 times the background, a 10% error in this estimate only contributes $\sim 3\%$ to the overall uncertainty of this calculation.

The reddening toward ϕ Per itself has been measured to be $E(B-V) = 0.20$ mag (Bohlin, Savage, & Drake 1978), although the intrinsic colors of the system may not be known well due to its complexity. A lower value for $E(B-V)$ is suggested by the total Hydrogen column density toward the system, $N(\mathrm{H\ I} + \mathrm{H_2}) = 3.7 \times 10^{20}$ cm^{-2} (Bohlin,

Savage, & Drake 1978), which leads to a reddening of $E(B-V) = 0.064$ mag. We have chosen to use this value in the calculations below. As a crude estimate of the extinction over the entire H II region, we can assume this value is constant and use the extinction curves of Clayton, Cardelli, & Mathis (1989). With no specific knowledge of the characteristics of the dust in this region, we adopt the standard value of $R_V = 3.1$ for the diffuse ISM. Using their formulae, at Hα the expected extinction is $e^{-2.7\ E(B-V)} = 0.84$. Using $E(B-V) = 0.20$ would imply extinction 40% larger.

The best estimate of L_c for this region is then 1.0×10^{47} ph s^{-1} using a distance of 220 pc. The two major uncertainties for this value are the $\sim 16\%$ uncertainty in the distance to the star, which translates into a $\sim 30\%$ uncertainty in our estimate of L_c, and the extinction correction, which assumes that the reddening toward the star is the same over the entire H II region. This second factor can be improved upon by future WHAM observations of Hβ. However, an additional uncertainty for the extinction correction that is more difficult to measure accurately is that we have neglected the fact that the scattering component of dust extinction affects extended objects much differently than point-like ones. While scattering normally removes photons from the line of sight, scattering within the H II region itself can reduce the effective extinction seen by an observer.

An estimate for n_e in a spherical H II region can be made from the ionizing flux-recombination balance equation,

$$L_c = \alpha_B\, n_e^2\, \frac{4\pi}{3} \mathcal{R}^3, \tag{2.14}$$

where α_B is the recombination coefficient. We use $\alpha_B = 3.10 \times 10^{-13}$ cm^3 sec^{-1}, interpolated from Osterbrock (1989) assuming a gas temperature of 8000 K. The estimate for n_e then becomes

$$n_e = 16.2 \sqrt{\frac{L_{c\,46}}{\mathcal{R}^3}}\ \text{cm}^{-3}, \tag{2.15}$$

where $L_{c\,46}$ is in units of 10^{46} ph s^{-1} and $\mathcal{R}$ is in pc. With $\mathcal{R} = 25$ pc and $L_{c\,46} = 10$, $n_e = 0.41$ cm^{-3}.

The complicated Be + sdO nature of the ϕ Per system may not lend itself to a straightforward application of stellar models designed for single star systems. The primary is believed to be the recipient of a considerable mass transfer from the (now) secondary sdO, resulting in a over-luminous (for its mass) B0.5 III-Ve primary with an extremely hot ($T_{\rm eff} > 50,000$ K), smaller companion (Gies et al. 1998).

A recent estimate of LyC luminosities for early-type stars calculated by Vacca, Garmany, & Shull (1996) predicts $L_c = 7.9 \times 10^{47}$ ph s^{-1} for a B0.5 V star and $L_c = 1.9 \times 10^{48}$ ph s^{-1} for a B0.5 III star, 8–19 times higher than our estimate from the H II region emission. Earlier calculations by Panagia (1973) gave $L_c = 4.0 \times 10^{46}$ ph s^{-1} and $L_c = 6.3 \times 10^{46}$ ph s^{-1} for luminosity classes V and III respectively, 1.5–2.5 times lower than our estimate. In addition, the companion sdO is believed to contribute nearly 17% additional flux at 1374 Å based on direct measurements of near-UV spectra (Gies et al. 1998), which would presumablely be higher below 912Å.

Even if the region were at twice the distance, it would still be difficult to reconcile our measured value of L_c with the latest theoretical values (Vacca et al. 1996). If these latest models are accurate for ϕ Per, possible explanations might be either that the H II region is actually density-bounded, despite the spherical shape and profile of its Hα emission, or that our extinction correction is too small. However, an average $E(B-V)$ of approximately 0.8 is required to increase our calculated flux by a factor of 8. Such a dramatic increase over the measured stellar reddening and that inferred from neutral Hydrogen seems unlikely.

The behavior of the other emission lines should be linked to the temperature and ionization properties of the region. Applying the same techniques for the WIM to this H II

region (see §2.3.3), we infer a temperature of 7,000 K to 8,500 K, noticeably higher than the 6,000 K to 7,000 K inferred for the ξ Per region (Figure 2.11). The ϕ Per region also appears to have a lower average S^+/S ratio than ξ Per. However, the large triangles in Figure 2.11 nearest the $S^+/S = 0.25$ line contain the majority of the Hα flux from the ξ Per region (NGC 1499) and have some of the lowest [S II]/[N II] values of our data.

2.5 Summary

We have presented the first comprehensive, velocity-resolved maps of [N II] and [S II] in the Galaxy. Combining the Hα maps from the WHAM Hα Sky Survey in this region, we draw the following conclusions:

1. We confirm earlier estimates of the distribution of Hα emission in the Perseus arm (Reynolds 1997). With continuous coverage from $b = -6°$ to $-35°$ ($|z| = 300$ to 1750 pc), we find that the electron distribution derived from the emission is described well by an exponential with a scale height of $H = 1.0 \pm 0.1$ kpc.

2. [S II]/Hα and [N II]/Hα emission in our Galaxy shows the same rise with increasing $|z|$ as found in observations of edge-on galaxies (Rand 1998; Golla et al. 1996). These ratios appear to be correlated with each other over a wide range of emission measures and $|z|$.

3. We suggest that the correlation between [N II]/Hα and [S II]/Hα can be attributed to the fact that changes in these ratios are primarily due to changes in electron temperature, and that scatter in the relationship is caused by variations in S^+/S. With this interpretation, we derive temperatures in the WIM of 6,000 K to 9,000 K and S^+/S ratios of 0.4 to 0.8. The average value of S^+/S appears to be lower in the Perseus arm within the studied region, which may be inconsistent with the photoionization models presented by Howk & Savage (1999) used to calculate S^{++}/S^+ ratios in the WIM. Higher ionization and lower temperatures are mostly found in the two H II regions. Differences in temperature between regions may be able to be directly confirmed by comparing the line widths of [S II] and Hα in our data (*e.g.* Reynolds 1985). In addition, several sightlines in this mapped region have been selected for further observations by WHAM to confirm these results. Observations of the faint, higher-level [N II] λ5755 transition combined with our λ6483 measurements can directly measure the electron temperatures in the emitting gas.

4. We explore a newly discovered H II region most likely excited by the B0.5III-Ve + sdO system ϕ Per. Its nearly circular appearance on the sky and square-root shaped emission profiles suggest a photon-bounded nebula in a fairly uniform environment, providing a rare opportunity to measure the LyC luminosity of a B star. We calculate the Lyman continuum luminosity needed to sustain the region to be 1.0×10^{47} ph s^{-1}. This region appears to be significantly warmer than the nearby O star H II region excited by ξ Per. WHAM has also explored Hα, [N II], and [S II] emission around the B1IV star α Vir, which will be presented elsewhere. Such studies may help probe the elusive Lyman continuum flux of early B stars and their contribution to the Galactic ionizing field.

References

Afflerbach, A., Churchwell, E., & Werner, M. W. 1997, ApJ, 478, 190

Anders, E. & Grevesse, N. 1989, Geochim. Cosmochim. Acta, 53, 197

Bohlin, R. C., Savage, B. D., & Drake, J. F. 1978, ApJ, 224, 132

Cardelli, J. A., Clayton, G. C., & Mathis, J. S. 1989, ApJ, 345, 245

Domgörgen, H. & Mathis, J. S. 1994, ApJ, 428, 647

Gies, D. R., Bagnuolo, W. G., Jr., Ferrara, E. C., Kaye, A. B., Thaller, M. L., Penny, L. R., & Peters, G. J. 1998, ApJ, 493,440.

Golla, G., Dettmar, R.-J., & Domgörgen, H. 1996, A&A, 313, 439

Greenawalt, B., Walterbos, R. A. M., & Braun, R. 1997, ApJ, 483, 666

Howk, J. C. & Savage, B. D. 1999, ApJ, in press

Kulkarni, S. & Heiles, C. 1987, in Interstellar Processes, eds. D. J. Hollenbach & H. A. Thronson, Jr. (Dordrecht: Reidel), 87

Martin, P. G. 1988, ApJS, 66, 125

Meyer, D. M., Cardelli, J. A., & Sofia, U. J. 1997, ApJ, 490, L103

Ogden, P. M. & Reynolds, R. J. 1985, ApJ, 290, 238

Osterbrock, D. E. 1989, Astrophysics of Gaseous Nebulae and Active Galactic Nuclei (Mill Valley: University Science Books)

Perryman, M. A. C. 1997, The Hipparcos and Tycho Catalogues, ESA SP-1200 (Noordwijk: ESA/ESTEC)

Panagia, N. 1973, AJ, 78, 929

Rand, R. J. 1998, ApJ, 501, 137

Rand, R. J. 1997, ApJ, 474, 129

Rand, R. J., Kulkarni, S. R., & Hester, J. J. 1990, ApJ, 352, L1

Reynolds, R. J. 1971, PhD Thesis, University of Wisconsin–Madison

Reynolds, R. J. 1980, ApJ, 236, 153

Reynolds, R. J. 1985a, ApJ, 294, 256

Reynolds, R. J. 1985b, ApJ, 298, L27

Reynolds, R. J. 1988, AJ, 96, 670

Reynolds, R. J. 1991, ApJ, 372, L17

Reynolds, R. J. 1997, in The Physics of Galactic Halos, eds. H. Lesch, R.-J. Dettmar, U. Mebold, & R. Schlickeiser (Akademie Verlag: Berlin), 57

Reynolds, R. J., Hausen, N. R., Tufte, S. L. 1998, & Haffner, L. M. 1998, ApJ, 494, L99

Reynolds, R. J. & Tufte, S. L. 1995, ApJ, 439, L17

Reynolds, R. J., Tufte, S. L., Kung, D. T., McCullough, P. R., & Heiles, C. 1995, ApJ, 448, 715

Sokolowski, J. 1994, preprint

Tufte, S. L. 1997, PhD Thesis, University of Wisconsin–Madison

Vacca, W. D., Garmany, C. D., & Shull, J. M. 1996, ApJ, 460, 914

Wang, J., Heckman, T. M., & Lehnert, M. D. 1997, ApJ, 491, 114

Table 2.1. Atmospheric Lines in [S II] and [N II] Observations

[S II]			[N II]		
Mean[a] (km s^{-1})	Width (km s^{-1})	Intensity (R)	Mean (km s^{-1})	Width (km s^{-1})	Intensity (R)
+26.8	0	0.06–0.38	+25	0	0.05–0.10
−72.2	10	0.12–0.29	−76	10	0.00–0.05
−113.2	0	0.03–0.14	(−40	0	0.05–0.10)[b]

[a]With respect to the geocoronal Hα line.

[b]Contaminated by Perseus arm emission. See text.

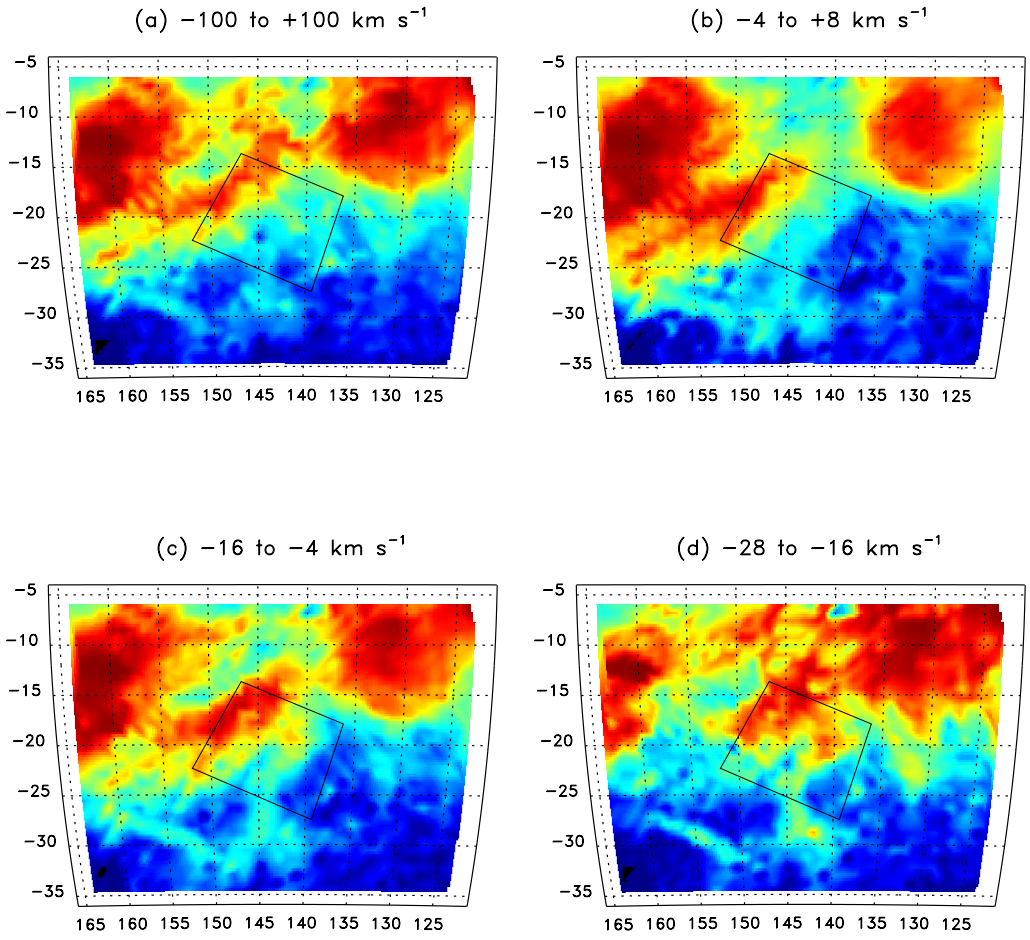


Fig. 2.1.— Hα Emission from the Orion Arm. These pseudo-color images show the integrated Hα emission in eight selected velocity bands. The axes are Galactic longitude and latitude. The overplotted box shows the location of the original Hα background survey in this region (see text). (*a*) $v_{\rm LSR} = -100$ to $+100$ km s^{-1}. (*b*) $v_{\rm LSR} = -4$ to $+8$ km s^{-1}. (*c*) $v_{\rm LSR} = -16$ to -4 km s^{-1}. (*d*) $v_{\rm LSR} = -28$ to -26 km s^{-1}.

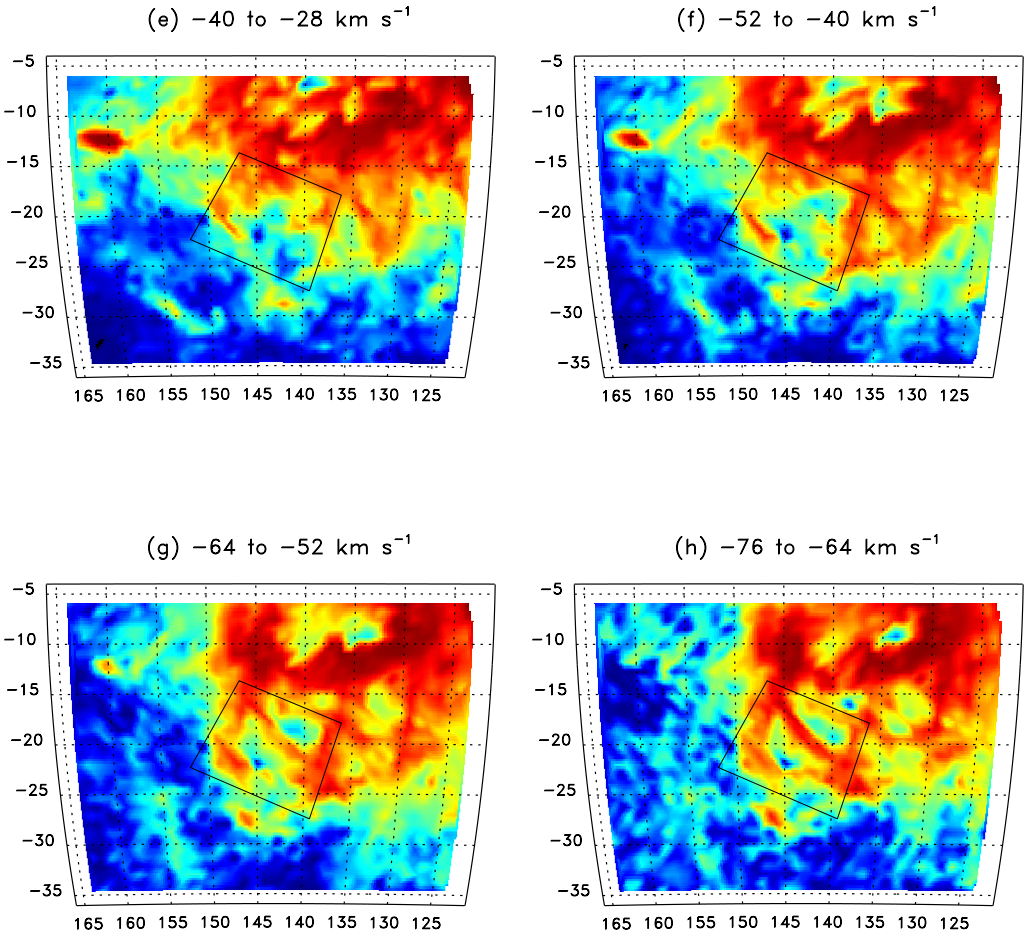


Fig. 2.1.— (cont.) Hα Emission from the Perseus Arm. (*e*) $v_{\rm LSR} = -40$ to -28 km s^{-1}. (*f*) $v_{\rm LSR} = -52$ to -40 km s^{-1}. (*g*) $v_{\rm LSR} = -64$ to -52 km s^{-1}. (*h*) $v_{\rm LSR} = -76$ to -64 km s^{-1}.

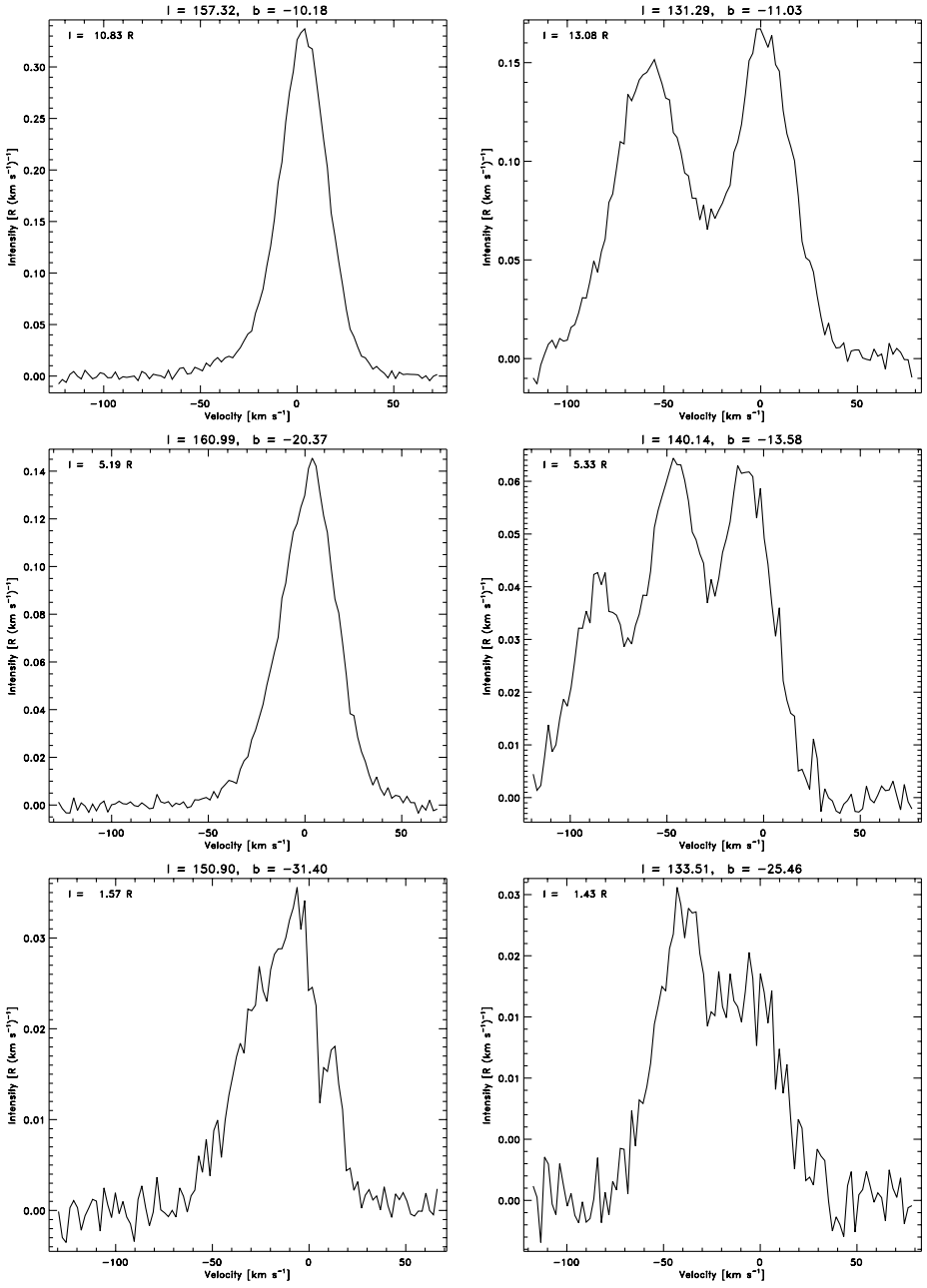


Fig. 2.2.— Sample Hα spectra from several directions are plotted as intensity versus LSR velocity. The total integrated intensity is labeled in the upper-left corner of each plot.

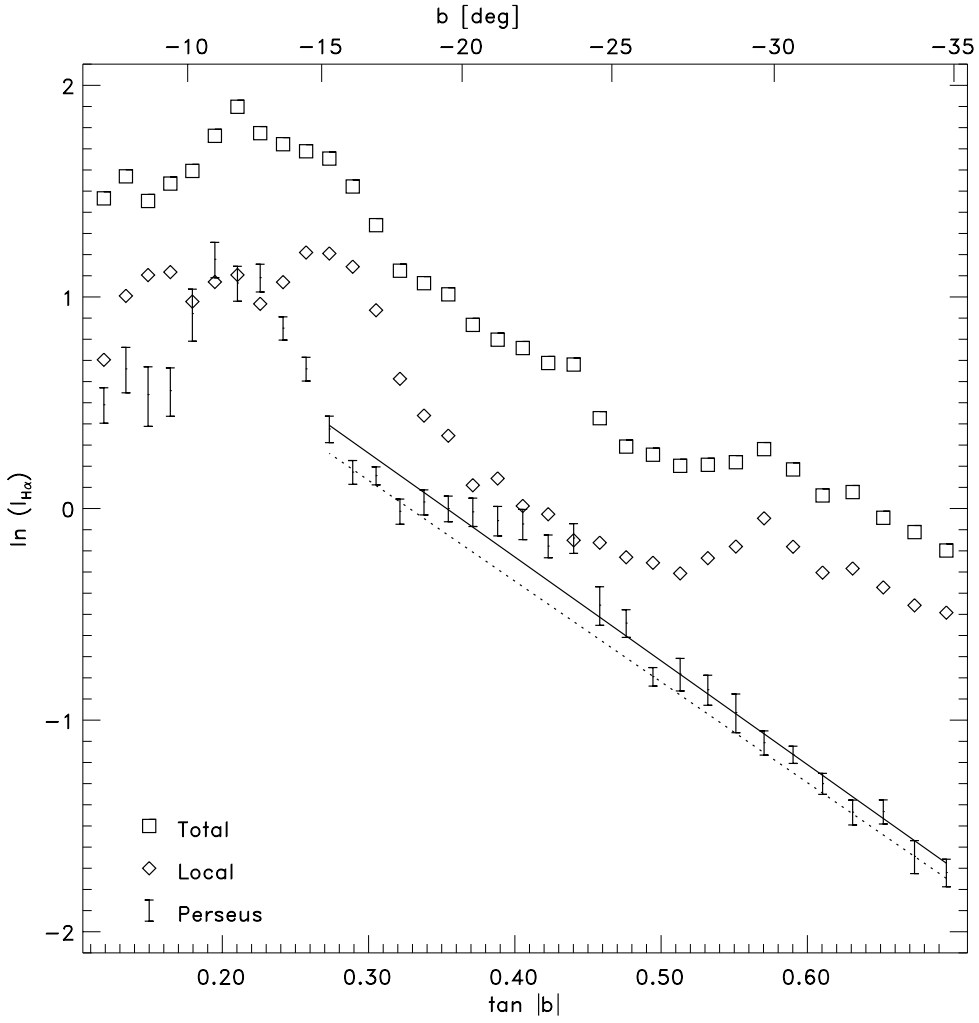


Fig. 2.3.— The natural logarithm of the median Hα intensity between $\ell = 125°$ and $152°$ is plotted versus the tangent of Galactic latitude. Total ($v_{\rm LSR} = -100$ to $+100$ km s^{-1}), Local ($v_{\rm LSR} = -25$ to $+100$ km s^{-1}), and Perseus arm ($v_{\rm LSR} = -100$ to -25 km s^{-1}) emission are denoted by the different symbols. A linear best fit to the Perseus arm emission above $b = -15°$ is displayed as a solid line. The dotted line is a fit to the lower envelope of the data (see §2.3.2).

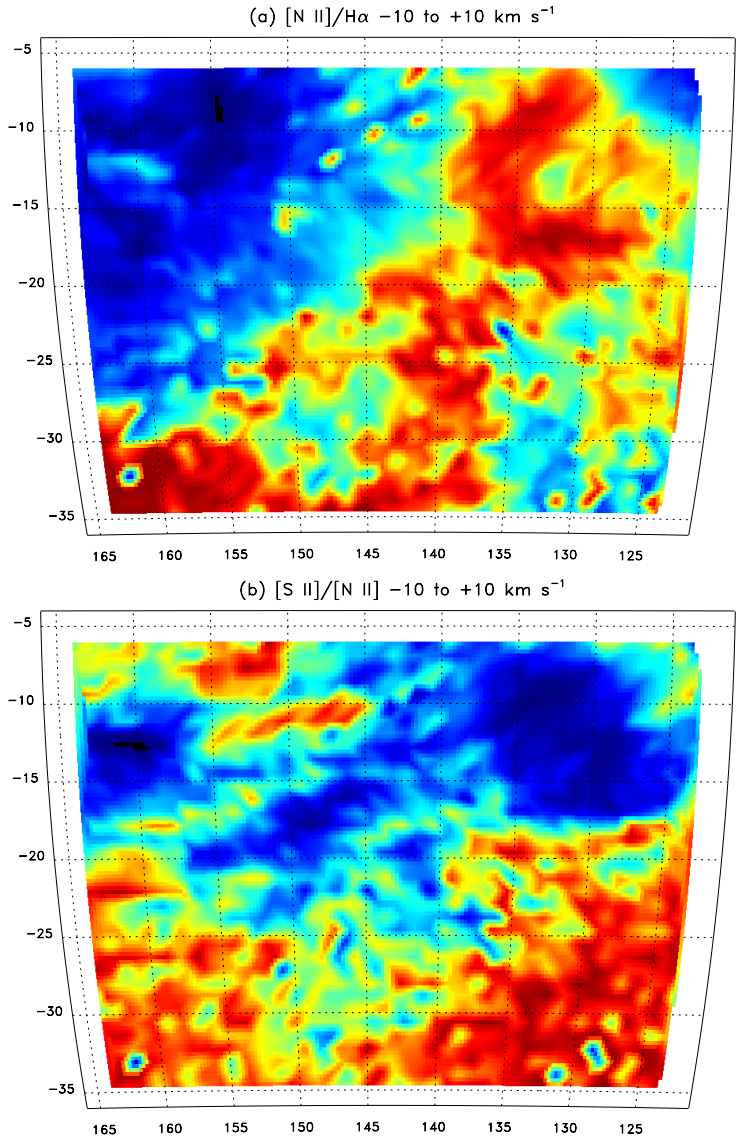


Fig. 2.4.— Emission line ratio maps of (a) [N II]/Hα and (b) [S II]/[N II]. The emission in each line has been integrated over $v_{\rm LSR} = -10$ to $+10$ km s^{-1}. In (a), values range from 0.14 (blue) to 2.9 (red). In (b), values range from 0.29 (blue) to 1.4 (red).

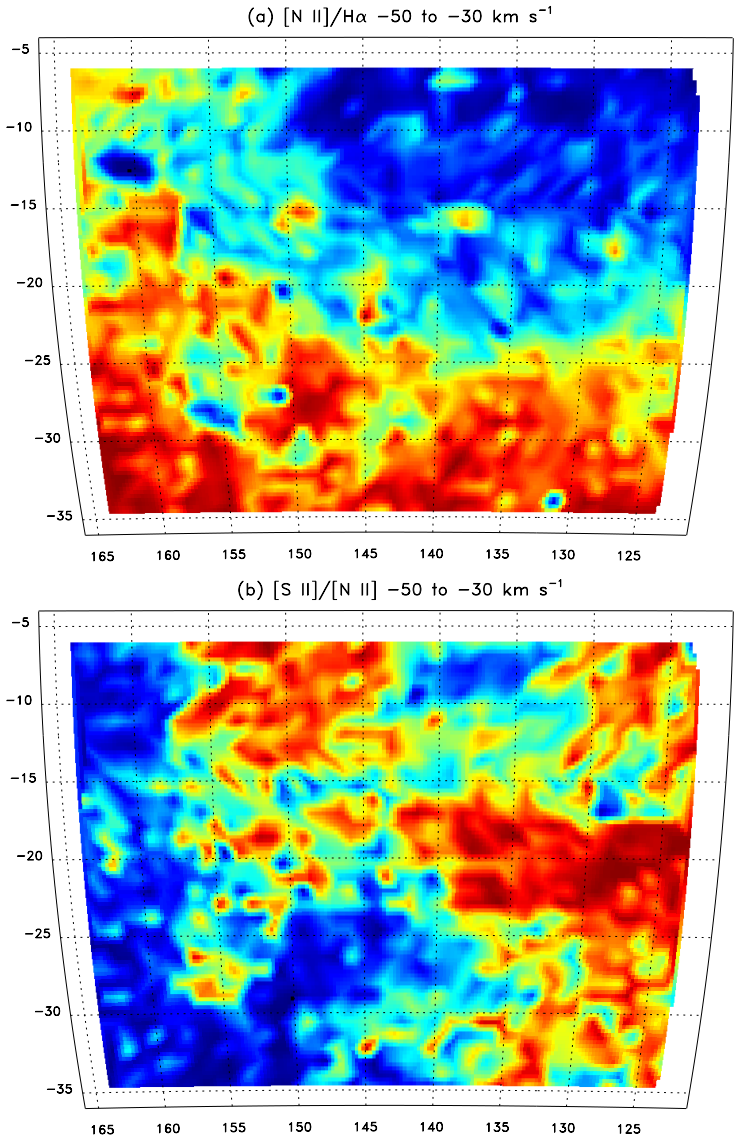


Fig. 2.5.— Emission line ratio maps of (*a*) [N II]/Hα and (*b*) [S II]/[N II]. The emission in each line has been integrated over $v_{\rm LSR} = -50$ to -30 km s^{-1}. In (*a*), values range from 0.28 (blue) to 4.5 (red). In (*b*), values range from 0.1 (blue) to 1.2 (red).

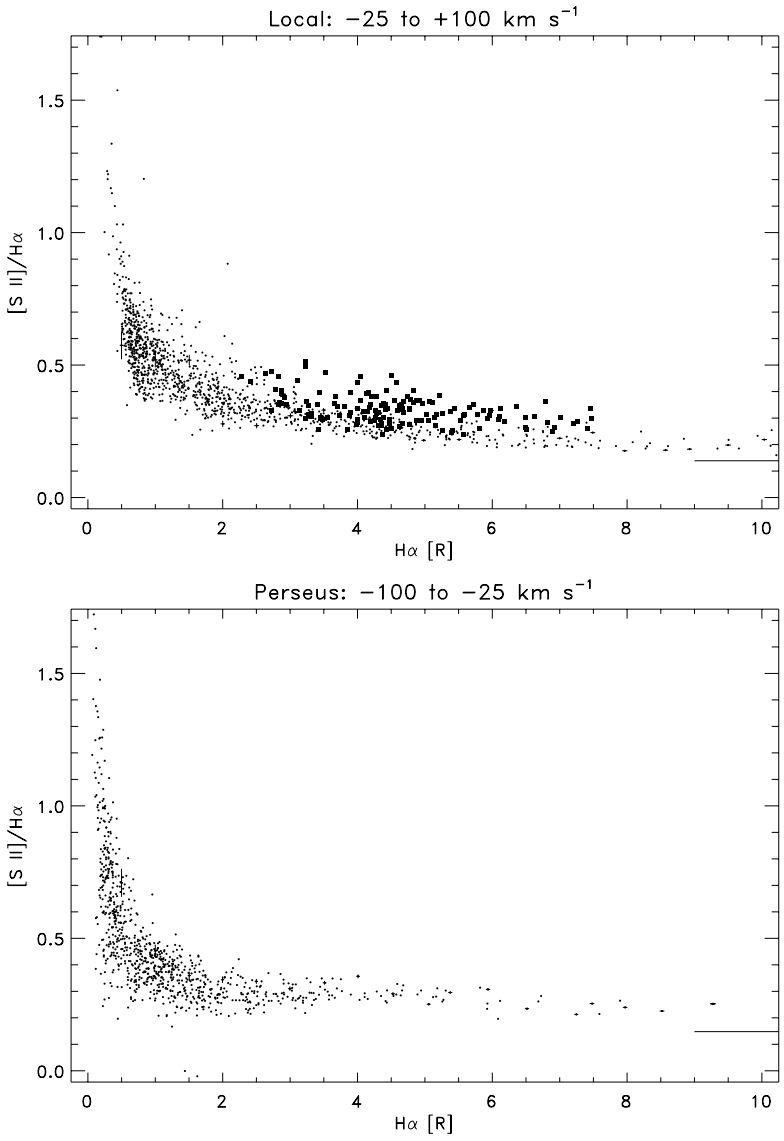


Fig. 2.6.— [S II]/Hα is plotted versus Hα intensity for both the Local and Perseus arm emission. For the Perseus arm, the longitude range has be restricted to $\ell = 125°$ through 152°. Crosses show representative error bars for select points. Filled squares denote pointings within 6.5° of the center of the H II region discussed in §2.4.2: $\ell = 131°$, $b = -11°$. The solid line denotes the average ratio of pointings with $I_{\mathrm{H}\alpha} > 50$ R (i.e. "classical" H II regions).

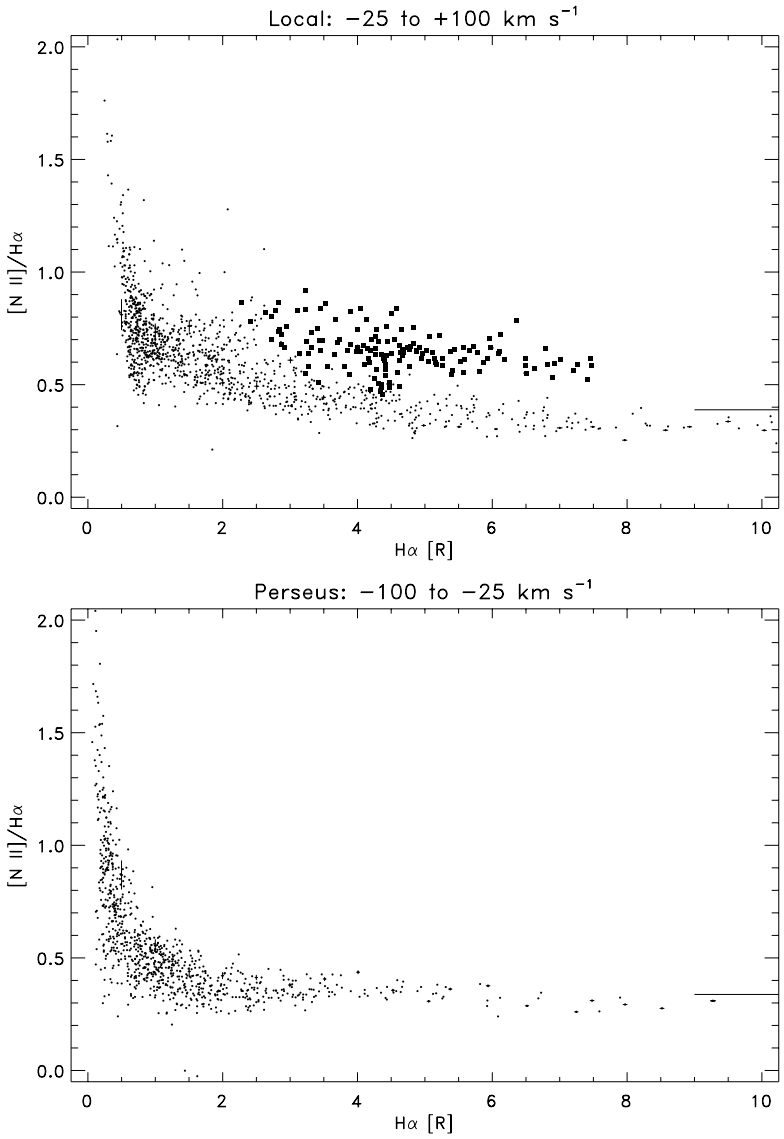


Fig. 2.7.— Same as Figure 2.7, but for [N II]/Hα versus Hα.

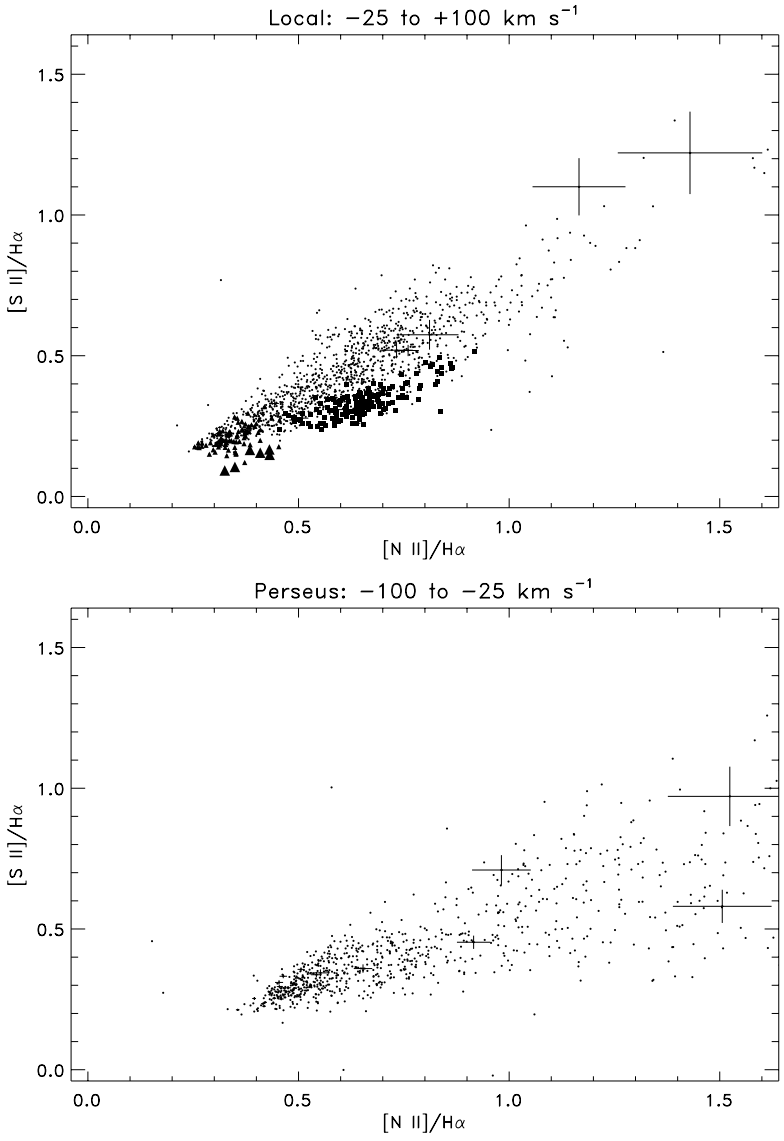


Fig. 2.8.— Same as Figure 2.7, but for [S II]/Hα versus [N II]/Hα. Additional plot symbols (triangles) denote pointings within 5° of the (rough) center of the ξ Per H II region: $\ell = 160°$, $b = -15°$.

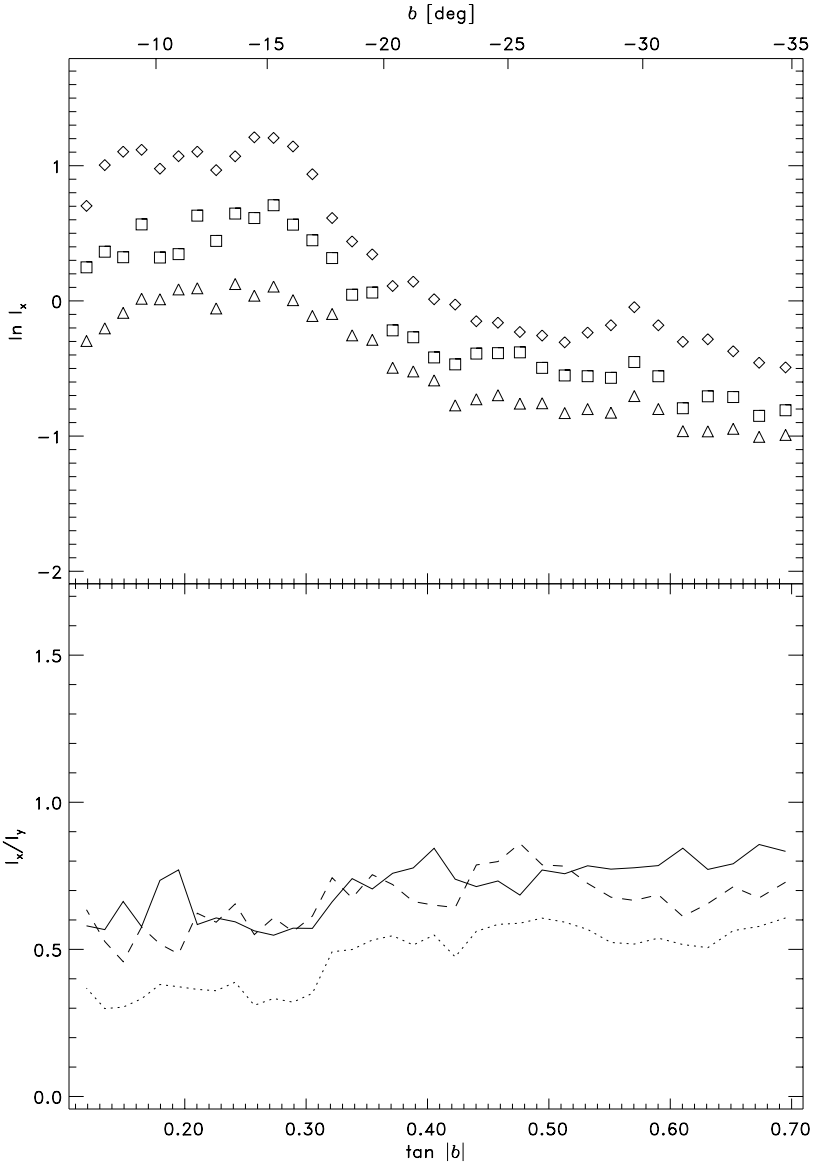


Fig. 2.9.— In the upper panel, the natural logarithm of the median intensity of Hα (diamonds), [S II] (triangles), and [N II] (squares) between $\ell = 125°$ and 152° is plotted versus the tangent of Galactic latitude. Intensities have been integrated over the velocity range $v_{\rm LSR} = -25$ to +100 km s^{-1}. The bottom panel plots three ratios: [S II]/Hα (dotted line), [N II]/Hα (dashed line), and [S II]/[N II] (solid line).

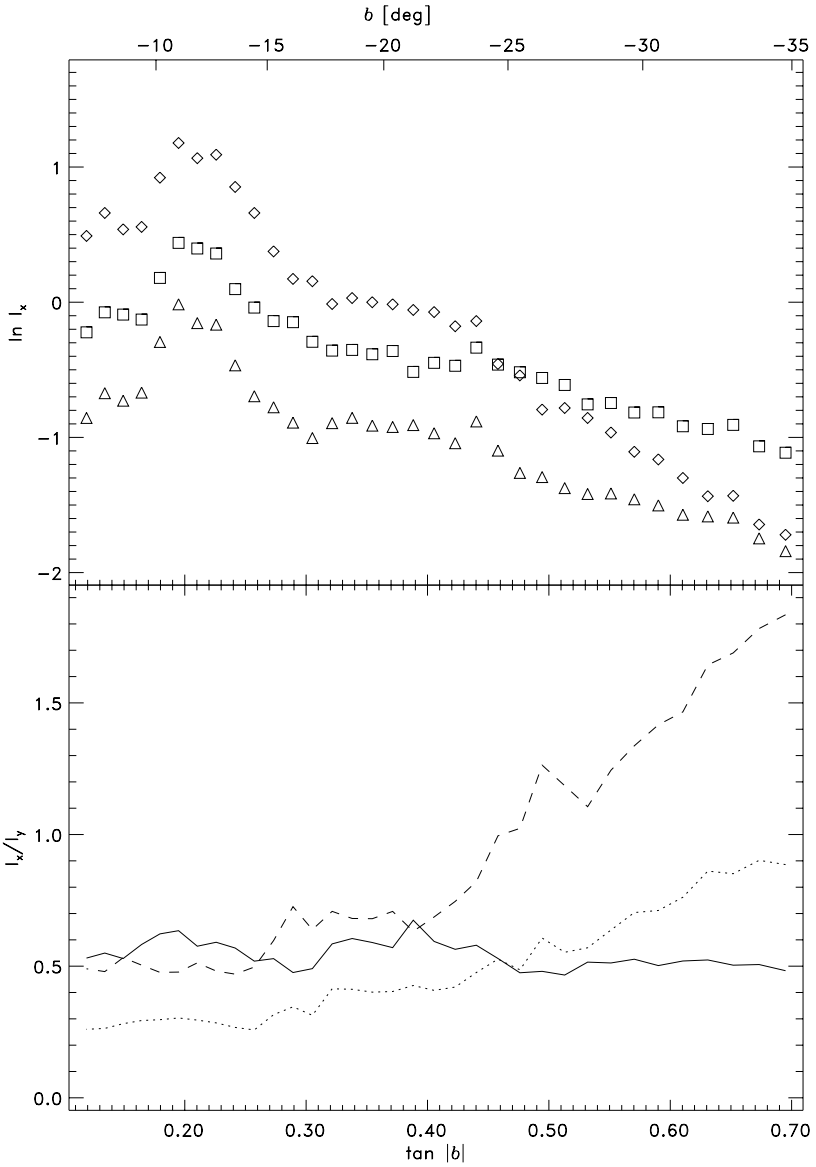


Fig. 2.10.— Same as Figure 2.9, except intensities have been integrated over the velocity range $v_{\rm LSR} = -100$ to -25 km s^{-1}.

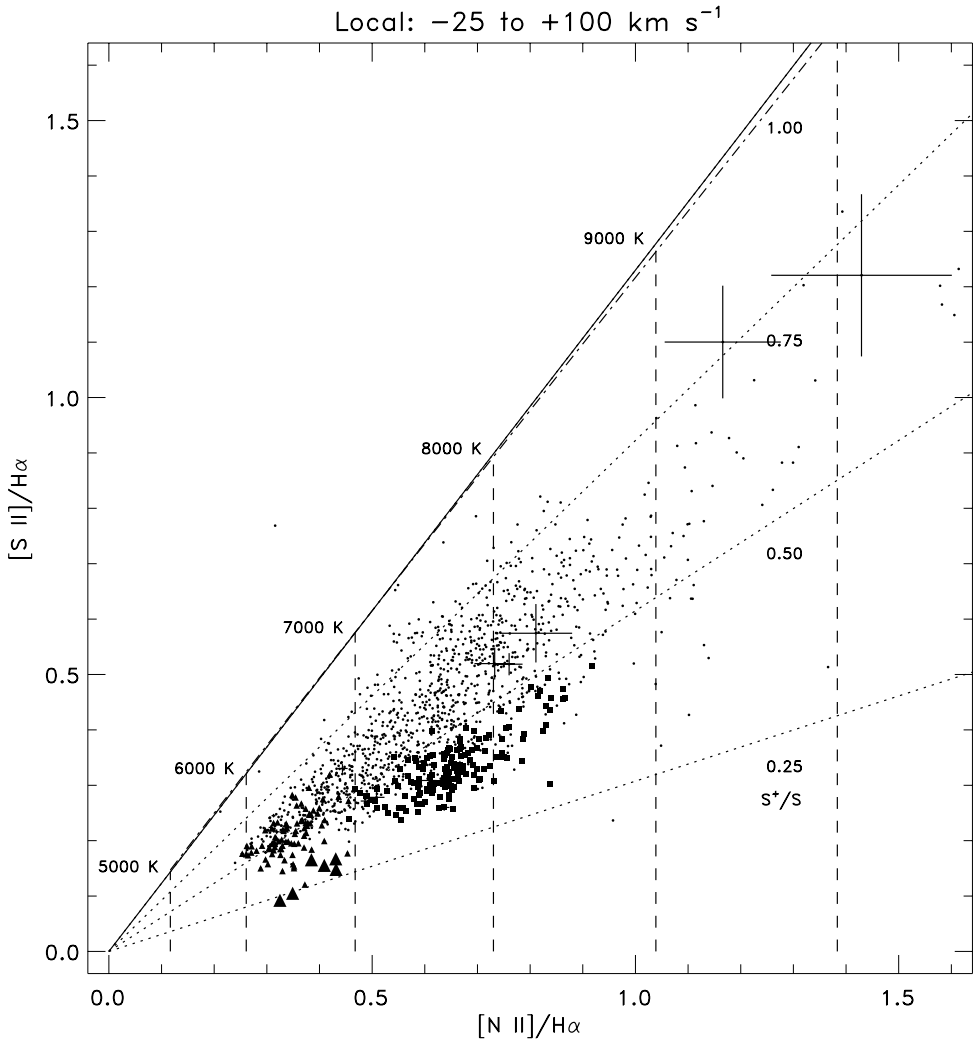


Fig. 2.11.— Same as Figure 2.8 for the Local arm only, except with a grid for inferred temperatures and S^+/S ratios.

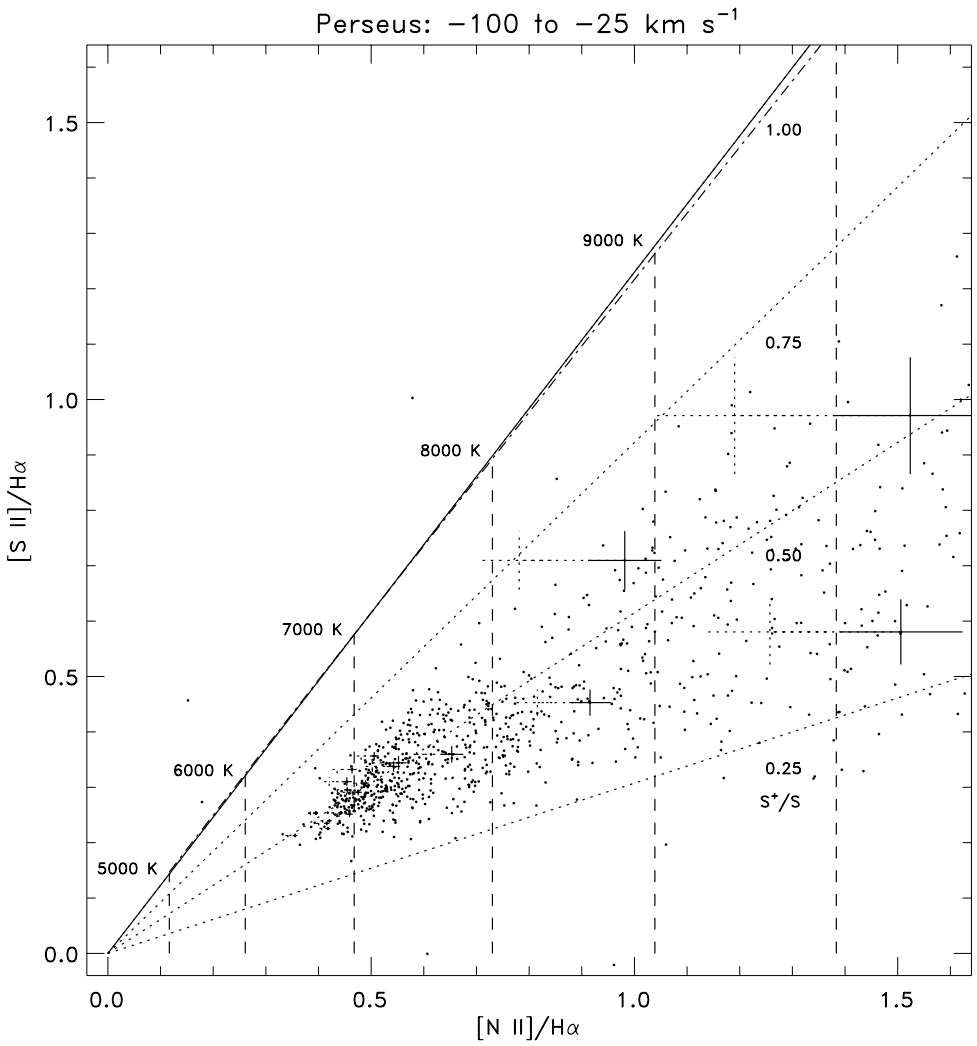


Fig. 2.12.— Same as Figure 2.8 for the Perseus arm only, except with a grid for inferred temperatures and S^+/S ratios.

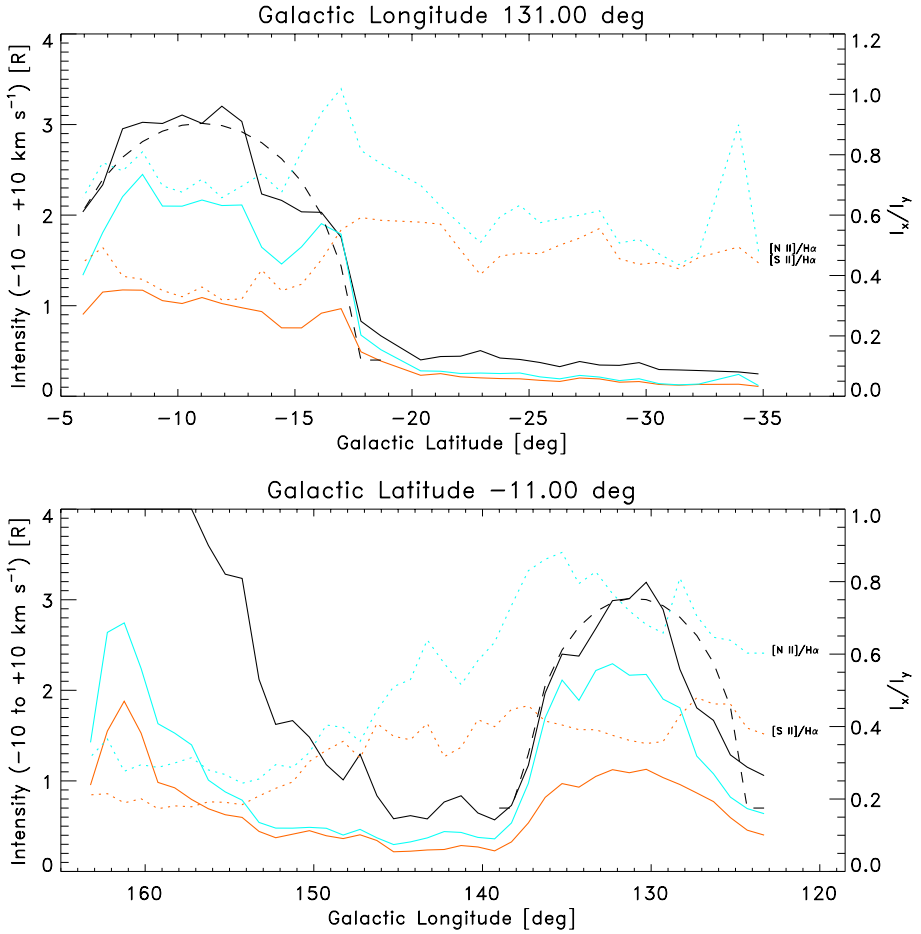


Fig. 2.13.— Emission line profiles through $\ell = 131°$ and $b = -11°$ (the center of the H II region discussed in §2.4.2). Hα (black), [S II] (red), and [N II] (blue) emission integrated over $v_{\rm LSR} = -10$ to $+10$ km s^{-1} are plotted against latitude and longitude. Dotted lines show [S II]/Hα (red) and [N II]/Hα (blue) emission line ratios. The dashed line represents the synthetic profile for a spherical H II region (see §2.4.2).

Chapter 3

Faint, Large-scale Hα Filaments in the Milky Way

Abstract

This chapter was originally published in the 1998 July 1 issue of The Astrophysical Journal (Letters) by Haffner, Reynolds, & Tufte, volume 501, page L83.

During the initial data reduction of the Wisconsin H-Alpha Mapper (WHAM) Hα Sky Survey, we have discovered several very long ($\sim 30°$–$80°$) filaments superimposed on the diffuse Hα background. These features have no clear correspondence to the other phases of the interstellar medium revealed by 21 cm, X-ray, IR, or radio continuum surveys, and they have no readily identifiable origin or source of ionization. In this letter, the data for two of these faint ($I_{H\alpha} \approx 0.5$–1.5 R) structures are presented. The first is an $80°$-long, $2°$-wide arch that extends nearly perpendicular to the Galactic plane at $\ell = 225°$ and attains a maximum latitude of $+51°$ near $\ell = 240°$ before reaching the southern boundary of our survey map at $\ell = 270°$, $b = +42°$. The vertical portion of this feature between $b = +10°$ and $+25°$ is associated with a single radial velocity component centered at $v_{\rm LSR} = +16$ km s^{-1} with a full width at half maximum of 27 km s^{-1}. A decrease in the velocity is observed from $b = +33°$ through $+48°$ as the feature arches toward higher Galactic longitudes. At this end, the emission component is centered near $v_{\rm LSR} = -20$ km s^{-1}. Where this feature appears to meet the Galactic plane near $\ell = 225°$, it is directly above the H II region surrounding CMa R1/OB1. A second filament consists of a $\sim 25°$–$30°$-long arc spanning $\ell = 210°$–$240°$ at $b = +30°$ to $40°$. The radial velocity of this feature increases systematically from 0 km s^{-1} at $\ell = 215°$, $b = +38°$ to $+18$ km s^{-1} at $\ell = 236°$, $b = +28°$. Both features have rather constant intensities along their entire lengths, ranging from 0.5–1.5 R (EM = 1–3 cm^{-6} pc) with no obvious trends.

3.1 Introduction

The Wisconsin H-Alpha Mapper (WHAM) survey is providing the first velocity-resolved map of the Hα emission from our Galaxy's diffuse interstellar medium. The combination of WHAM's sensitivity (< 0.1 R) and velocity resolution (12 km s^{-1}) reveals new details about the large-scale structure and kinematics of the Warm Ionized Medium (WIM). Studies of faint emission structures in the WIM may help us understand the distribution and morphology of the ionized gas and may even provide direct evidence of ionization sources. In this letter, we present the discovery of two large, faint filaments in our Galaxy.

3.2 Observations

WHAM consists of a dedicated 0.6-m, all-sky siderostat connected to a 15-cm, double-etalon Fabry-Perot spectrometer. The optical design delivers a spectrum covering a 200 km s^{-1} radial velocity interval from a one-degree circular patch of sky. For the Hα sky survey, approximately 35,000 spectra were obtained above $\delta = -20^\circ$ with the one-degree diameter beam centered on a $0.^\circ98 \times 0.^\circ85$ grid in ℓ and b. The integration time for each one-degree pixel was 30 seconds, resulting in a signal-to-noise ratio of about 30 in background continuum regions of the spectrum. This allows the detection of sources as faint as 0.1 R (1 R $= 10^6/4\pi$ ph cm^{-2} s^{-1} ster^{-1} or 2.4×10^{-7} ergs cm^{-2} s^{-1} ster^{-1} at Hα) in a single exposure. The etalons are configured to provide a spectral resolution of 12 km s^{-1}, which is sufficient to identify and remove atmospheric lines in the spectra and fully resolve the Hα emission-line profiles from warm gas ($T \sim 8000$ K) in the Galaxy. A detailed description of the instrument design is given by Tufte (1997).

Presented here are nearly 3800 of these spectra extracted from the WHAM Hα Sky Survey. They cover the region of the sky from $\ell = 200^\circ$ to 270° and $b = -10^\circ$ to $+60^\circ$ above $\delta = -20^\circ$. Most of these spectra were observed by WHAM from 1997 February through 1997 May. These observations are designated "O1" below. A small portion (145 spectra) from $\ell = 253^\circ$ to 270° and $b = +47^\circ$ to $+60^\circ$ was observed in January 1998 and are labeled "O2" below. Standard WHAM data reduction, including bias subtraction, reflected ring subtraction, annular-summing, and flat fielding, was used to create these spectra (Chapter 2; Haffner, Reynolds, & Tufte 1999).

Atmospheric emission lines are a significant source of contamination in WHAM spectra. The brightest of these, with intensities ranging from 2–13 R, is the geocoronal Hα line emitted in the earth's upper atmosphere. Since the earth's orbital velocity changes the location of the velocity frame of the Local Standard of Rest (LSR) with respect to the geocentric velocity frame, most directions in the sky were observed when the geocoronal line was separated by at least 20 km s^{-1} from the LSR. This separation makes it easy to resolve the relatively narrow (6–8 km s^{-1} FWHM) geocoronal line from the Galactic Hα emission and minimize its effect. The data presented here have velocity separations of the geocoronal line from the LSR that range from -24 km s^{-1} to -42 km s^{-1} (O1) and $+14$ km s^{-1} to $+25$ km s^{-1} (O2). A single Gaussian component has been fitted and subtracted from these spectra to remove the geocoronal line.

Two other much fainter atmospheric emission lines, believed to be extremely weak OH emission, are present in the spectra. The first is located 71 km s^{-1} to the red of the geocoronal line ($v_{\rm LSR} = +27$ to $+45$ km s^{-1} in O1); it has a width of 23.5 km s^{-1} and varies in intensity from 0.05 to 0.36 R. Deeper observations and the wide line width suggest that this feature may be a pair of atmospheric lines. The second is located 38 km s^{-1} to the blue of the geocoronal line ($v_{\rm LSR} = -64$ to -82 km s^{-1} in O1); it has a width of 9.4 km s^{-1} and varies in intensity from 0.04 to 0.13 R. For this study, the red sky line provides the most

contamination near the LSR in O1, and it has been removed by approximating it as a single Gaussian component. Variations in the line intensities are most severe from night to night. Our corrections account for intensity variations over 30-minute periods, which are typically 0.02 R. Other faint atmospheric lines are present in O2 even further to the blue from the geocoronal line. These features will not be discussed here since they do not affect our study near the LSR.

A first-order polynomial fits the sky background well within our 200 km s^{-1} bandpass. The typical level of the subtracted background is approximately 0.03–0.07 R (km s^{-1})$^{-1}$ or 1.4–3.2 R Å^{-1}, which is dominated by atmospheric continuum emission above $|b| = 30°$. Individual stars within the one-degree beam brighter than sixth magnitude contribute significantly to the background in several directions. Some of the spectra in these directions also contain an Hα absorption line from the stars. These pointings are most noticeable in Figure 3.1 as isolated one-degree diameter depressions in the otherwise smooth emission at higher Galactic latitudes.

Absolute intensity calibration is accomplished by frequent observations of nebular sources. All WHAM intensities are tied to the absolute intensity measurement of the North American Nebula (NAN; NGC 7000), 850 R within a 50′ beam centered at $\ell = 85.^{\circ}60$, $b = -0.^{\circ}71$, as determined by Scherb (1981). Since we have yet to apply the gamut of intensity calibrations to our data, relative intensities quoted here are accurate to about 10%. The systematic uncertainty in the absolute scale (i.e., the intensity of NGC 7000) is believed to be approximately 15%.

3.3 Results

Figure 3.1 displays four velocity integrated images of Hα emission from our selected region of the sky. The two filaments of interest are most easily seen in the narrow (12 km s^{-1}) velocity interval images, although their overall structure can also be seen on the "broad-band" map (Figure 3.1a). The vertical portion of the longest filament (hereafter Filament 1) is most prominent in the map centered on $v_{\rm LSR} = +20$ km s^{-1} (Figure 3.1d), stretching nearly perpendicular to the Galactic plane along $\ell = 225°$. It then extends toward higher Galactic longitudes, turning over near $b = +50°$ while shifting to more negative velocities in Figures 3.1c and 3.1b. A second long filament (Filament 2) can been seen as an arc extending across the images near $b = +30°$ to $+40°$. Its peak emission moves from $\ell = 220°$ in the $v_{\rm LSR} = -20$ km s^{-1} map (Figure 3.1b) to $\ell = 235°$ in the $v_{\rm LSR} = +20$ km s^{-1} map (Figure 3.1d). Other filaments are also apparent, including the feature running from $\ell = 205°$, $b = +25°$ to $\ell = 220°$, $b = +30°$. In this letter we focus primarily on the 80°-long Filament 1.

An ℓ-v map is presented in Figure 3.2 along $b = +25°$. From this representation, Filament 1 appears to be a narrow ($\lesssim 2°$) feature at $\ell = 225°$ that is offset in velocity from the smooth emission present near the LSR at other Galactic longitudes. An analysis of the spectra reveal that this velocity offset is about +18 km s^{-1}. The spectrum of Filament 1 averaged over six of the WHAM pointings taken around $\ell = 225.^{\circ}5$, $b = +25.^{\circ}5$ is displayed in Figure 3.3 as a dashed line. Because the velocity separation of the two components ($\Delta v \approx 20$ km s^{-1}) is less than the typical Doppler width of WIM Hα lines (FWHM $\approx 20 - 30$ km s^{-1}), a straightforward two-component fit of this spectrum is not well constrained. Instead, we attempt to isolate the filament from gas near the LSR by subtracting an estimate of the general WIM contribution in this direction. The spectra of two "background" regions taken at the same Galactic latitude are also displayed in Figure 3.3 as dotted lines. These directions are averages of nine pointings around $\ell = 232.^{\circ}0$, $b = +25.^{\circ}5$ and 12 pointings around $\ell = 220.^{\circ}5$, $b = +25.^{\circ}5$. An average of these spectra is subtracted from the average filament spectrum to produce the final filament-only spectrum in Figure 3.3 (solid line). The resulting component is fit well by a single Gaussian with a mean of $+18 \pm 2$ km s^{-1}, a

FWHM of 27 ± 6 km s^{-1}, and an intensity of 1.2 ± 0.2 R.

Using this method, we have determined fit parameters for several directions along Filament 1 and 2 and present the results in Table 3.1. Regions where the filaments cross are deliberately excluded. The accuracy of the filament component parameters depends primarily on how well the background regions represent the true emission near $v_{\rm LSR} = 0$ km s^{-1} in the filament direction. The errors of the parameters listed in Table 3.1 are conservatively estimated by examining subtractions of different background directions from the filament spectra. The fitting errors are an order of magnitude smaller and do not contribute significantly. Note the velocity gradients in both filaments with increasing Galactic longitude, decreasing from $v_{\rm LSR}$ +18 km s^{-1} to -25 km s^{-1} in Filament 1 and increasing from $v_{\rm LSR}$ 0 km s^{-1} to +18 km s^{-1} in Filament 2. Also note the nearly constant Hα intensities and line widths.

3.4 Discussion

The intensities in Table 3.1 are converted to emission measures using the formula:

$$\mathrm{EM}\ (\mathrm{cm}^{-6}\ \mathrm{pc}) = 2.75\ T_4^{0.9}\ I_{\mathrm{H}\alpha}\ (\mathrm{R})\ e^{2.2\,E(B-V)}, \tag{3.1}$$

where T_4 represents the temperature of the emitting gas in units of 10^4 K. With typical values for the temperature of the WIM gas, $T_4 = 0.8$ (Reynolds 1985), an Hα intensity of 1 R corresponds to an EM of 2.25 cm^{-6} pc. Since we are examining mostly high-latitude features, we expect corrections for interstellar extinction to be small. No such correction has been applied to the data presented here.

To derive further physical parameters for the filaments, we must make an assumption about the distances to them. Some evidence suggests that the lower part of Filament 1 is at a distance of about 1 kpc, based on its radial velocity and possible association with CMa R1/OB1. The lower portion has a radial velocity of +16 km s^{-1}, which is consistent with a kinematic distance of approximately 1 kpc at this Galactic longitude for a value of Oort's Constant $A = 16$ km s^{-1} kpc^{-1} (Mihalas & Binney 1981). Unfortunately, this argument is weakened by the radial velocities of the filament's high-latitude portion, which are "forbidden" in the Galactic rotation model. However, in Figure 3.1d ($v_{\rm LSR} = +20$ km s^{-1}), the vertical portion of Filament 1 appears to end in the prominent H II region surrounding the star-forming association CMa R1/OB1. In fact, the center of the brighter, arc-shaped, Hα emission features in this H II region, as seen on the Palomar Sky Survey red plates, is at $\ell = 225°$, $b = -1°$ (Reynolds & Ogden 1978). Also, the velocity centroid of the H II region (Table 3.1) is similar to that of the first 15°–20° of the filament away from the plane. Unless the agreement between the spatial and velocity information of these two regions is a coincidence, we can use the distance of the H II region as an estimate of the distance to the filament. The distance to the CMa OB1 association has been determined photometrically by Clariá (1974) to be 1150 ± 140 pc, consistent with a kinematic distance of 800-1100 pc for the Hα emitting gas in the region (Reynolds & Ogden 1978). In this letter, we adopt a distance of 1 kpc for Filament 1 but include $d_1 = d/1$ kpc in the derived parameters.

At a distance of 1 kpc, the vertical extent of Filament 1 ($b \approx +51°$) translates to a vertical height above the Galactic mid-plane, Z, of $1200\,d_1$ pc and a width ($\approx 2°$) of $35\,d_1$ pc. If we assume the filament is a cylinder of uniform density gas of width L, then the emission measure,

$$\mathrm{EM}\ (\mathrm{cm}^{-6}\ \mathrm{pc}) = \int_0^L n_e^2\,dl = n_e^2 L, \tag{3.2}$$

of the feature can be used to estimate the density. For Filament 1, where $L = 35\ d_1$ pc and EM ≈ 1.1 cm^{-6} pc, $n_e = 0.18\ d_1^{-1/2}$ cm^{-3}. The typical column density through the

filament is $N_e = 1.9 \times 10^{19}\ d_1^{1/2}$ cm^{-2}. The mass of the material in the filament's vertical section can be estimated by $1.4\ m_H\ Z\ L^2\ n_e = 9.2 \times 10^3\ d_1^{5/2}$ M$_\odot$, where the factor 1.4 is a correction for helium. If the filament is photoionized, our observed EM implies an incident ionizing flux of at least α_B EM $= 1.0 \times 10^6$ ph cm^{-2} s^{-1}. The hydrogen recombination rate within the filament is given by $\alpha_B\ n_e^2 = 1.0 \times 10^{-14}\ d_1^{-1}$ cm^{-3} s^{-1}, implying that the power required to sustain this rate throughout the volume of the filament is $(\alpha_B\ n_e^2\ Z\ L^2) \times 13.6$ eV $= 9.4 \times 10^{36}\ {d_1}^2$ erg s^{-1}. The value of α_B used in these calculations, 3.10×10^{-13} cm^3 sec^{-1}, is interpolated from Osterbrock (1989) assuming a gas temperature of 8000 K.

The narrow shape and location of Filament 1, particularly the coincidence in location and radial velocity of one end of the filament with an energetic source in the plane (CMa R1/OB1), suggest one possibility for its origin—a jet-like ejection from the association. However, given the length of the filament at the distance of CMa R1/OB1, the apparently low velocities associated with it (Table 3.1), and the near constant Hα intensity profile along its entire length, it is difficult to reconcile a scenario in which ionized hydrogen is being ejected from CMa R1/OB1 with the gas's short recombination times. A parcel of ionized gas at these temperatures and densities will recombine in $t_r = (\alpha_B\ n_e)^{-1} = 1.8 \times 10^{13}\ d_1^{1/2}$ s $= 5.7 \times 10^5\ d_1^{1/2}$ yr. To reach the observed height and remain ionized, the gas would need to be ejected at speeds in excess of $Z/t_r = 1400\ d_1^{1/2}$ km s^{-1}. We see no evidence for such speeds in our data. Furthermore, we would expect a significant gradient in the filament's intensity as a function of height above the Galactic plane, since gas at larger distances from the plane has had more time to recombine.

If another source is responsible for maintaining the ionization of Filament 1, an ejection scenario could still be plausible. If the filament's arc shape is caused by free-fall of ejected gas back to the Galactic plane, an initial velocity of about 70 km s^{-1} is required to reach the observed height above the plane at the distance of CMa R1/OB1. Such speeds agree better with the measured filament component velocities in Table 3.1, particularly when projection effects are considered. However, the filament's length would then require that the ejecting source be more than 3×10^7 yr old. This number can be compared to estimates of 3×10^6 yr for the age of CMa OB1 by Clariá (1974) and 7.6×10^5 yr for the age of a supernova put forth by Herbst & Assousa (1977) as being responsible for generating the ring-shaped Hα nebulosity in the vicinity of CMa OB1/R1 and for being the progenitor of star formation in the R1 association. In this scenario, a diffuse ionization source is probably required to maintain a constant intensity along the filament, since the growing distance from CMa R1/OB1 would produce an intensity gradient if it were the sole source. The efficiency of leaking Lyman continuum radiation from the disk is a longstanding problem for ionizing a thicker layer of the Galaxy. However, Bland-Hawthorn & Maloney (1998), Dove & Shull (1994), and Miller & Cox (1993) have argued that a substantial ionizing flux can diffuse into the Galaxy's halo from the disk. The required ionizing flux of at least 1.0×10^6 ph cm^{-2} s^{-1} is consistent with these models.

Several other phenomena may produce large, faint filaments. Large-scale, kinematic Galactic structures such as superbubbles, chimneys, or worms have been popular explanations for filamentary structures seen in H I as well as Hα (*e.g.* Koo, Heiles, & Reach 1992; Reynolds & Ogden 1979). The velocity gradient of Filament 1 is outside the range expected from a simple model of Galactic rotation and therefore may be evidence for a dynamical influence on the filament. However, the observed velocity gradient is inconsistent with this feature being the edge of an expanding shell, since a shell's projected edges should be at a constant radial velocity. Furthermore, for the two cases presented here, we find no obvious correlation between these Hα filaments and emission at other wavelengths, including H I 21 cm, Rosat All-Sky Survey X-Ray, and IRAS bands, making it difficult to relate them

to previously identified H I "worms" and superbubbles. Since the Leiden/Dwingeloo H I survey is sensitive to below 5×10^{18} cm^{-2} (Harmann & Burton 1997), the ionized column density of the filament, 2×10^{19} cm^{-2}, suggests that the gas is fully ionized. Other possibilities include a suggestion by Dupree & Raymond (1983) that faint, ionized trails of ionized hydrogen could be produced by high-velocity white dwarfs. However, the recombination time discussed above suggests unreasonable velocities for the star.

In summary, we present the discovery of two long, faint Hα filaments at high latitudes from the WHAM Hα survey. Their origin is not yet identified, but the existence of such features may help to explain processes responsible for the maintenance of the general WIM layer. As additional portions of the Hα survey are reduced, new clues about the nature of these structures may be revealed. We plan to follow these observations with [S II] and [N II] observations of this region. Additional observations will provide information about the gas's temperature and ionization state, which are useful in narrowing the kinds of processes that can be producing these filaments.

We thank Kurt Jaehnig and Jeff Percival of the University of Wisconsin's *Space Astronomy Lab* for their dedicated engineering support of WHAM; Nikki Hausen, Mark Quigley, and Brian Babler for data reduction support; and Trudy Tilleman for essential night-sky condition reports from Kitt Peak, which have made remote observing possible. We acknowledge the use of NASA's *SkyView* facility (http://skyview.gsfc.nasa.gov), located at NASA Goddard Space Flight Center and the SIMBAD database, operated at CDS, Strasbourg, France. This work is supported by the National Science Foundation through grants AST9619424 and AST9122701.

References

Bland-Hawthorn, J. & Maloney, P. R. 1998, ApJ, submitted

Clariá, J. J. 1974, A&A, 37, 229

Dove, J. B. & Shull, J. M. 1994, ApJ, 430, 222

Dupree, A. K. & Raymond, J. C. 1983, ApJ, 275, L71

Haffner, L. M., Reynolds, R. J., & Tufte, S. L. 1998, in preparation

Hartmann, D. & Burton, W. B. 1997, Atlas of Galactic Neutral Hydrogen (New York: Cambridge University Press)

Herbst, W. & Assousa, G. E. 1977, ApJ, 217, 473

Koo, B.-C., Heiles, C., & Reach, W. T. 1992, ApJ, 390, 108

Mihalas, D. & Binney, J. 1981, Galactic Astronomy: Structure and Kinematics, 2nd edition (New York: W. H. Freeman & Co.)

Miller, W. W., III & Cox, D. P. 1993, ApJ, 417, 579

Osterbrock, D. E. 1989, Astrophysics of Gaseous Nebulae and Active Galactic Nuclei (Mill Valley: University Science Books)

Reynolds, R. J. 1985, ApJ, 294, 256

Reynolds, R. J. & Ogden, P. M. 1978, ApJ, 224, 94

Reynolds, R. J. & Ogden, P. M. 1979, ApJ, 229, 942

Scherb, F. 1981, ApJ, 243, 644

Tufte, S. L. 1997, Ph.D. Thesis, University of Wisconsin–Madison

Table 3.1. Fitted Filament Parameters

Position (ℓ, b)	# of Avg'd Spectra	Mean (km s^{-1})	FWHM (km s^{-1})	Intensity (R)
		Filament 1		
(225.°5, + 0.°0)[a]	5	+14.0±0.1	32.5±0.1	59.1±0.1
(227.°0, +10.°2)	9	+18±2	23±4	0.9±0.1
(225.°5, +12.°7)	9	+16±2	24±4	1.1±0.4
(225.°0, +15.°3)	6	+18±2	22±3	0.6±0.1
(225.°0, +17.°8)	6	+16±3	26±6	0.6±0.2
(225.°0, +20.°4)	6	+16±1	33±2	1.4±0.1
(225.°5, +25.°5)	6	+18±2	27±6	1.2±0.2
(227.°3, +33.°1)	12	+9±3	20±2	0.6±0.1
(227.°3, +35.°7)	10	+6±1	22±1	0.5±0.1
(227.°3, +38.°2)	10	+4±3	25±2	0.5±0.4
(227.°3, +40.°8)	11	0±4	24±6	0.4±0.2
(227.°3, +43.°3)	11	−1±3	23±2	0.6±0.1
(229.°3, +45.°9)	9	−8±1	25±1	0.4±0.1
(231.°6, +48.°4)	11	−18±1	22±3	0.5±0.1
(234.°0, +50.°5)	7	−22±1	22±4	0.6±0.1
(239.°0, +51.°0)	9	−25±3	26±4	0.6±0.1
		Filament 2		
(215.°3, +36.°5)	6	0±3	31±1	1.2±0.4
(217.°8, +37.°5)	6	−1±1	26±1	1.3±0.3
(220.°5, +37.°5)	6	−2±1	27±2	1.0±0.4
(230.°3, +35.°5)	6	0±4	22±6	0.4±0.2
(232.°3, +34.°8)	6	+1±1	29±1	0.7±0.1
(234.°3, +33.°0)	6	+13±1	31±1	0.4±0.1
(236.°0, +30.°5)	8	+18±2	37±1	1.0±0.1

[a]This direction is toward the H II region surrounding CMa R1/OB1.

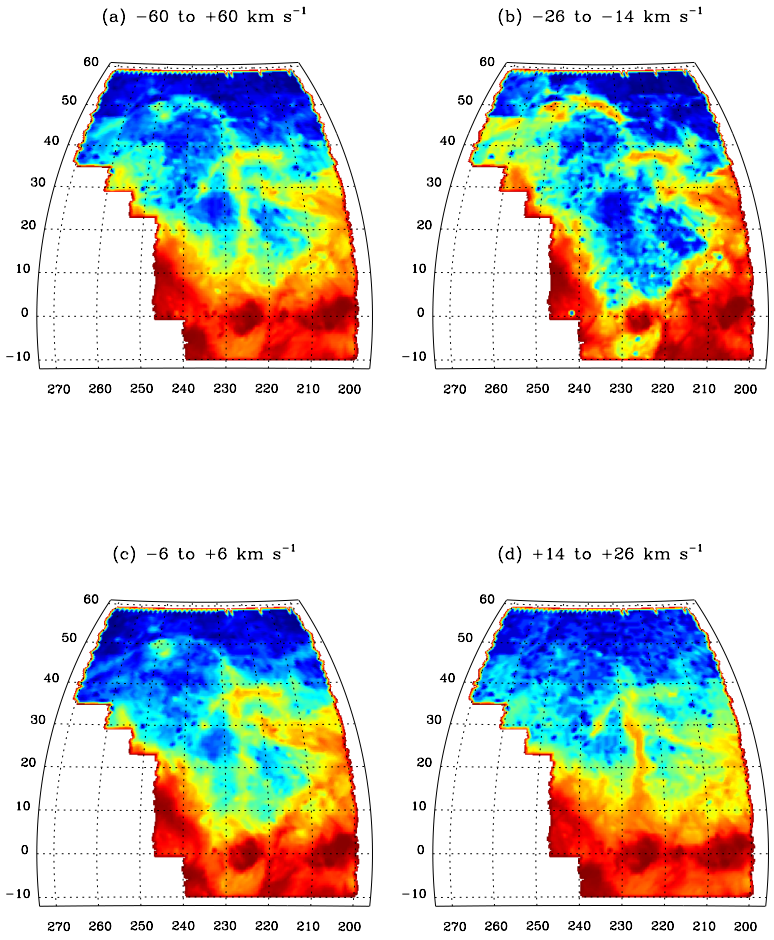


Fig. 3.1.— A portion of the WHAM Hα Sky Survey. These pseudo-color images show the integrated Hα emission in four selected velocity bands. The axes are Galactic longitude and latitude. (*a*) $v_{\rm LSR} = -60$ to $+60$ km s^{-1}. (*b*) $v_{\rm LSR} = -26$ to -14 km s^{-1}. (*c*) $v_{\rm LSR} = -6$ to $+6$ km s^{-1}. (*d*) $v_{\rm LSR} = +14$ to $+26$ km s^{-1}. "Holes" in the images are pointings uncorrected for a bright stellar absorption line.

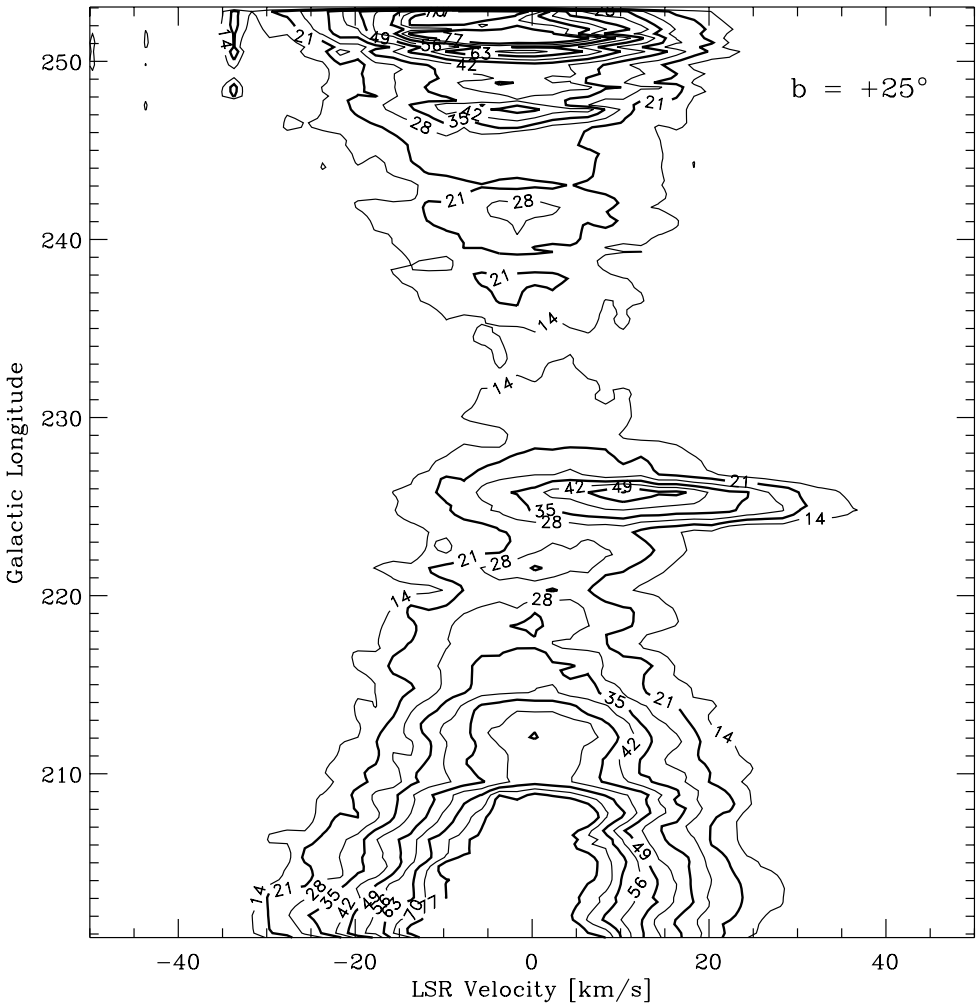


Fig. 3.2.— Longitude-Velocity intensity map at $b = +25°$. Contour levels are in units of 10^{-3} R $(\mathrm{km\ s^{-1}})^{-1}$. Filament 1 crosses $b = +25°$ at $\ell = 225°$.

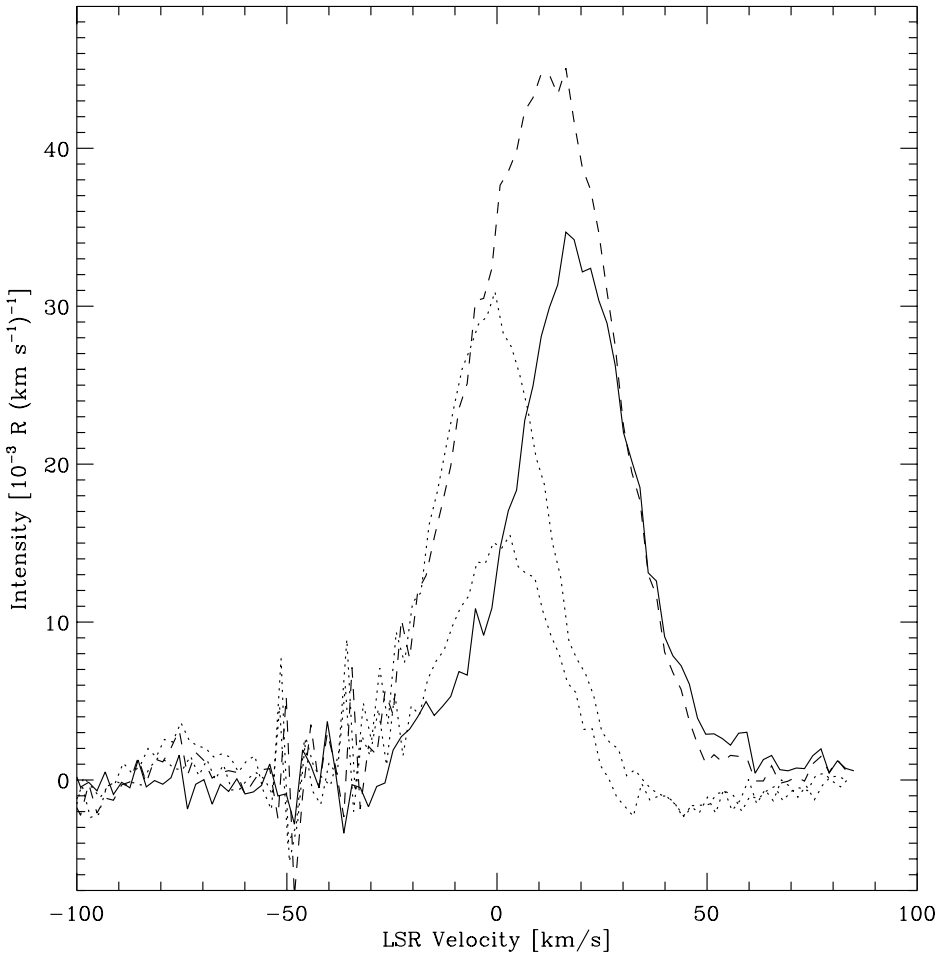


Fig. 3.3.— Filament and background spectra at $b = +25\overset{\circ}{.}5$. Intensity is plotted against $v_{\rm LSR}$. Atmospheric lines have been removed. The dashed line is the original emission toward the filament, the dotted lines are two background directions, and the solid line is the background-subtracted filament emission (see text). The increased noise near -40 km s^{-1} is a residual of the geocoronal Hα line, whose peak emission is centered near that velocity.